



Challenges of Retrofitting Existing Aircraft With Next-Generation Powertrains

Matteo Guidotti*, Sai Sankalp Shekar*, Aidan R. Molloy*, Dhairy Mehta†, Ava Cipriani†, Aadit Kolar†, and Matthew A. Clarke‡

University of Illinois Urbana-Champaign, Urbana, IL 61801

This study investigates the challenges and near-term limitations associated with implementing hybridization strategies in existing narrow-body aircraft, with a particular focus on mild parallel hybrid-electric architectures operating on alternative fuels, including PtL-SAF, LPG, LNG, and LH₂. The analysis examines how fuel selection and limited electrification influence aircraft performance, emissions, and operational characteristics for a retrofitted Airbus A220-100 platform. A Latin Hypercube Sampling approach is employed to explore the design space and evaluate cost per revenue passenger-kilometer, hybridization trends, mission-level emissions, and turnaround time. For each configuration, onboard fuel and energy storage systems are resized within the constraints of the baseline aircraft outer mold line, accounting for mass and volume limits. Uncertainty in the medium-fidelity chemical reaction network used for combustor emissions modeling is quantified using a Monte Carlo simulation. The results show that the optimal hybridization strategy follows the inverse trend of engine specific fuel consumption, with increased electric assistance during takeoff and climb and minimal contribution during cruise. However, with current battery technology, the economic benefits of mild hybridization are limited, with cost reductions observed only for the LH₂ configuration. Across all fuels, mild hybridization produces negligible changes in total mission CO₂-equivalent emissions per revenue passenger kilometer. Operationally, turnaround times remain comparable to conventional narrow-body operations for all configurations, with battery recharging identified as the primary constraint. Overall, the findings provide system-level insight into the trade-offs and practical feasibility of retrofitting existing narrow-body aircraft with hybrid-electric and alternative-fuel propulsion technologies.

Nomenclature

<i>BPR</i>	= Bypass Ratio	<i>PSR</i>	= Perfectly Stirred Reactor
<i>CO₂e</i>	= CO ₂ equivalent	<i>PZ</i>	= Primary Zone
<i>C.G.</i>	= Center of Gravity	<i>S_{ref}</i>	= Reference Wing Area
<i>CRN</i>	= Chemical Reactor Network	<i>SZ</i>	= Secondary Zone
<i>DA</i>	= Dilution	<i>SM</i>	= Slow Mode
<i>EI</i>	= Emission Index	<i>T_{SL}</i>	= Thrust at Sea Level
<i>f</i>	= Fraction	<i>UHC</i>	= Unburned Hydrocarbons
<i>FAR</i>	= Fuel to Air Ratio	<i>n_c</i>	= Number of compressor stages
<i>FL</i>	= FL	<i>V</i>	= Volume
<i>L</i>	= Length	φ	= Equivalence Ratio
<i>LNG</i>	= Liquid Natural Gas	ϕ	= Hybridization Ratio
<i>LPG</i>	= Liquid Petroleum Gas	μ	= Friction coefficient
<i>MTOW</i>	= Maximum Take-Off Weight	<i>W</i>	= Tank Width
<i>MZFW</i>	= Maximum Zero Fuel Weight	<i>h</i>	= Tank End Cap Height
<i>OWE</i>	= Operating Empty Weight	<i>H</i>	= Tank Height
<i>OPR</i>	= Overall Pressure Ratio		
<i>PFR</i>	= Plug Flow Reactor		

*Graduate Student, Department of Aerospace Engineering, AIAA Student Member.

†Undergraduate Student, Department of Aerospace Engineering, AIAA Student Member.

‡Assistant Professor, Department of Aerospace Engineering, AIAA Member.

I. Introduction

AVIATION contributes approximately 2% of the 35 billion metric tons of anthropogenic emissions. With global air traffic growing at an average rate of 5.2% per year [1], the environmental impact of air transportation continues to intensify. Over the past five decades, climate-driven pressures, including sea-level rise, extreme weather events, and economic disruption, have accelerated the need for rapid decarbonization across all sectors, including aviation [2]. The industry has responded with notable progress: improvements in lightweight composite structures, aerodynamic performance, and air-traffic management have delivered average fuel-efficiency gains of roughly 2.1% per year, exceeding the initial 1.5% target [3]. Yet growth in global passenger demand is projected to outpace these incremental gains, underscoring the need for more transformative propulsion and energy-system solutions.

One promising decarbonization pathway involves replacing conventional Jet-A with alternative energy carriers that offer lower life-cycle greenhouse gas emissions. Liquefied Petroleum Gas (LPG), Liquefied Natural Gas (LNG), and liquid hydrogen (LH_2) each provide unique technical benefits, such as reduced carbon intensity and cleaner combustion byproducts, particularly when produced from renewable sources. However, their integration introduces significant engineering challenges related to cryogenic or pressurized storage, fuel-system safety, thermal management, and certifiability. LPG requires pressurized tanks with substantial structural reinforcement. LNG and LH_2 , by contrast, must be stored in well-insulated cryogenic tanks that add mass and introduce boil-off management requirements, which are difficult to accommodate within slender wing geometries. As a result, cabin or cargo volume must often be repurposed for fuel storage, reducing passenger capacity and altering weight-and-balance characteristics, an effect examined in this study.

From an operational perspective, these fuels exhibit contrasting advantages and limitations. LNG infrastructure is widespread across the United States due to extensive industrial and trucking applications [4], yet its liquefaction and distribution remain energetically costly. LPG benefits from mature global supply chains and low storage temperatures but provides lower volumetric energy density than Jet-A. Hydrogen offers the strongest emissions-reduction potential, but at the cost of deeply cryogenic storage, increased tank volume, stringent leak-prevention requirements, and complex airport-side handling. These trade-offs highlight the systems-level nature of integrating alternative fuels into existing airframes.

In addition to fuel switching, hybrid-electric propulsion has emerged as a compelling near-term approach to reducing fuel burn and emissions. Parallel hybrid architectures, where electrical power supplements but does not replace, turbine shaft power, are particularly attractive because they maintain reliance on proven gas-turbine technology while enabling partial electrification. However, hybridization introduces complexity in powertrain integration, thermal management, systems engineering workflows, safety analyses, and concept-of-operations development. Despite low energy and power densities, thermal regulation, and the need for continuous diagnostics, batteries are still the front runner in the technologies considered to provide this electrical energy. Progress in industry, such as megawatt-class electric machines, high-specific-power inverters, and flight demonstrators from companies including Airbus, Ampaire, and ZeroAvia, has accelerated technology readiness, yet significant integration and certification hurdles remain. A growing body of literature demonstrates hybridization's potential benefits for efficiency, climb performance, and noise reduction [5], while other studies show the challenges associated with battery sizing, mission adaptability, and the diminishing returns imposed by mass growth [6]. The big question remains: does it make sense to hybridize from an economics standpoint?

For the purpose of this study, an existing single-aisle fleet is analyzed, and both alternative fuels and hybrid-electric systems are introduced as retrofits within the outer mold line (OML). Consequently, new fuel tanks, cryogenic systems, electrical components, and high-voltage distribution architectures are fit within the baseline A220-100 geometry. This creates strong couplings among fuel storage volume, system mass, aircraft stability margins, payload capacity, and internal passenger-layout modifications (LOPA). These geometric and operational constraints propagate through mission performance, turnaround time, and revenue passenger-kilometer (RPK) economics. Despite substantial research on hybrid-electric aircraft and alternative fuels, comparatively little work has examined the integrated systems-engineering trade space of retrofitting today's single-aisle transports.

Given the tightly coupled nature of propulsion, fuel storage, mission modeling, and airline operations, fuel type and hybridization level drive a cascade of design decisions that span combustor thermodynamics, hybrid-propulsor behavior, internal-volume allocation, stability constraints, operational feasibility, and emissions characteristics. This paper evaluates these interactions using a hierarchical system-of-systems framework (Fig. 1) to quantify how alternative fuels and varying degrees of hybridization influence aircraft performance and operations.

The main objectives of this work are to:

- Assess the feasibility of families of mild-hybrid retrofit variants combining multiple hybridization levels with candidate alternative fuels, while keeping the aircraft OML and MTOW fixed;

- Quantify the impact of fuel choice and hybridization on mission performance;
- Evaluate changes in direct-use emissions, including CO₂, CO, NO_x, and H₂O, using a medium-fidelity chemical reaction network with uncertainty quantification;
- Identify operational implications, such as refueling, charging, and turnaround-time, that influence the real-world viability of alternative-fuel hybrid retrofits.

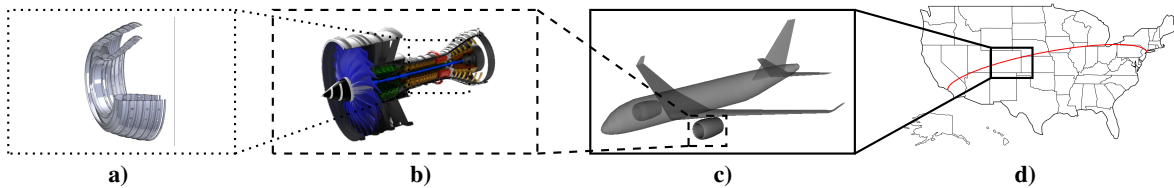


Fig. 1 Hierarchical system architecture considered in this work: (a) medium-fidelity combustor subsystem; (b) hybrid-turbofan engine system of interest; (c) aircraft-level system of systems; and (d) flight operations domain representing the family of systems.

II. Short-Haul Concept of Operations

A. Narrow-Body Aircraft Selection

The aircraft selected for an investigation on powertrain hybridization was the Airbus A220-100 (formerly the Bombardier CS100). With a maximum range of 3,600 nautical miles and a maximum takeoff weight of 63,100 kilograms, this single-aisle twin-engine jet aircraft commenced operations in July 2016. In addition to its recent entry into service, the aircraft was chosen due to its large market share in the sub-150-seat single-aisle jet aircraft market, seen in Figure 2a, making it a prime candidate to benchmark against best-in-class systems. The aircraft is equipped with Pratt & Whitney PW1500G geared turbofan engines, incorporating fly-by-wire flight controls, a carbon composite wing, an aluminum-lithium fuselage, and optimized aerodynamics to enhance fuel efficiency. According to the Bureau of Transportation Statistics [7], a mission range of 1500 nmi corresponds to approximately the 96th percentile of all A220-100 flights operated to or from the United States. Frequent flights, along with a quick survey of trajectories pointing towards cruise altitudes between 25,000ft and 32,000ft, imply that climb performance and turnaround time are crucial to operating the aircraft efficiently and profitably. A three-dimensional rendering of A220, including its standard LOPA, is depicted in Figure 2b. The accuracy of this geometry was checked against its Airport Planning Manual (APM) [8], which has 3-view drawings, dimensions, weights, and performance metrics like the Payload-Range diagram.

After verifying the more prominent, publicly documented parameters such as outer mold line dimensions, including span and aspect ratio, powertrain specifications like design thrust and engine dimensions, and mass properties, including MTOW, OEW, and MZFW, lesser-known attributes such as airfoil characteristics and section twist were adjusted to

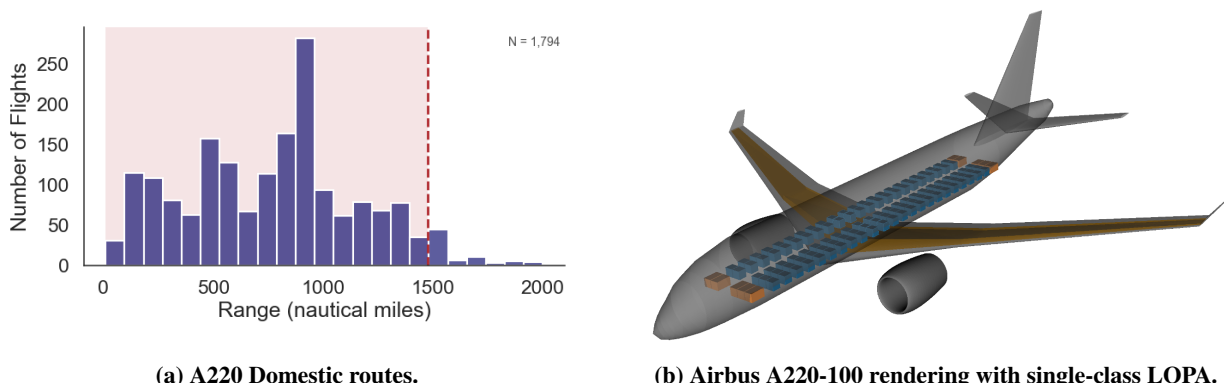


Fig. 2 A220 domestic flight operations and geometry.

ensure the computational model of the aircraft closely matched official performance metrics. Old transonic airfoil sections from the 737 on the Airfoil Tools database [9–12] were utilized for the wings. The general LOPA presented in the APM is also utilized. This is also illustrated in Fig. 2b.

B. Mission Specification

The mission shown in Figure 3 below depicts a notional flight profile of the aircraft. Table 1 outlines the representative block time comprised of flight profile segments adopted for the aircraft in this study. These mission segments define key parameters such as altitude, airspeed, and vertical rate across each phase of flight. Flight data from commercial flights obtained from the online database FlightAware [13] was used to verify that these segments closely resemble commercial ones. Segments 1 and 17 denote the duration during which the aircraft is stationed at the gate for deplaning, boarding, refueling, and servicing. Segments 2 and 16 represent the taxiing durations to and from the departure runway, respectively. Segments 3 and 15 illustrate the aircraft's acceleration and deceleration on the runway. Segments 4 to 15 denote the flight duration, encompassing many phases of ascent, a level cruise, and a descent segment. This study focuses on evaluating a hypothetical flight operation, so a reserve segment is not included in the model.

Table 1 Flight segments of a nominal mission of an Airbus A220.

No.	Segment Type	Altitude [ft]	Airspeed [kts]	Climb Rate [ft/min]	Note
1	Boarding/Deplaning/Refuel	0	0	0	Gate
2	Ground Taxi	0	10	0	16-min taxi
3	Ground Accel.	0	10-140	0	Runway $\mu = 0.03$
4	Takeoff Roll	0-35	140-150	250	In-Air
5	Initial Climb	35-1,500	150-250	1,800	In-Air
6	Climb to FL 50	1,500-5,000	250-275	1,700	In-Air
7	Climb to FL 100	5,000-10,000	275-300	1,500	In-Air
8	Accel. to Climb Speed	10,000	300-400	0	In-Air
9	Climb to FL 300	10,000-30,000	400-450	1,500	In-Air
10	Constant Speed Cruise	30,000	450	0	In-Air
11	Descent to FL 100	30,000 -10,000	450-250	-1,850	In-Air
12	Final Descent	10,000-1,500	250-150	-650	In-Air
13	Approach	1,500-400	150	-600	In-Air
14	Landing	400-0	150	-300	In-Air
15	Ground Decel./Braking	0	150-10	0	Runway $\mu_{brake} = 0.4$
16	Ground Taxi	0	10	0	10-min taxi
17	Boarding/Deplaning/Refuel	0	0	0	Gate

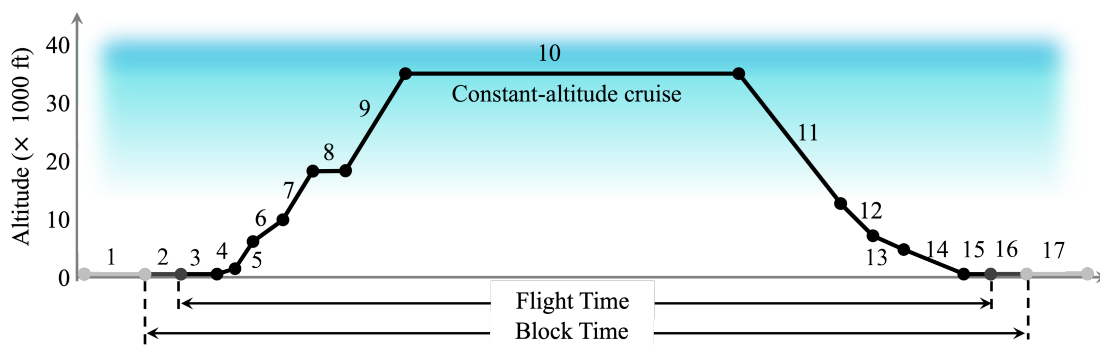


Fig. 3 Illustration of A220 flight profile.

III. Aircraft Modeling and Hybrid Powertrain Subsystem Integration

A. Computational Modeling and Simulation Framework

To elucidate the impact of integrating alternative fuels into a parallel hybrid powertrain architecture, the modeling and simulation of retrofitted aircraft is performed in RCAIDE [14], an open-source, Python-based platform. It supports the modular design and simulation of aerospace systems by treating each layer (combustor, engine, aircraft, and mission) as a subsystem nested within a higher-level system of interest.

This paper emphasizes geometric and spatial constraints of component interaction, deviating from many studies that take a simplistic approach to representing the integration of key elements of this powertrain. Shown in Figures 4a and 4b are the fuel line and electrical power networks of this aircraft, respectively, equipped elements that are commonly overlooked at the conceptual level, including valves, emergency buses, transformer rectifier units (TRUs) and auxiliary power units (APUs). These diagrams depict a system-level representation composed of interconnected elements that model the physical and functional subsystems of the propulsion architecture. These components are categorized into five primary functional groups: Converters, Distributors, Modulators, Propulsors, and Sources. Converters are responsible for transforming energy from one form to another to yield a desired output. This category includes the key thermodynamic elements of the propulsion cycle, namely the fan, compressor, combustor, turbine, and nozzle, which together define the operating characteristics of the engine. Each converter module corresponds to a distinct physical process (e.g., compression, combustion, expansion) and is modeled using a polytropic-based formulation, as detailed by Cantwell [15].

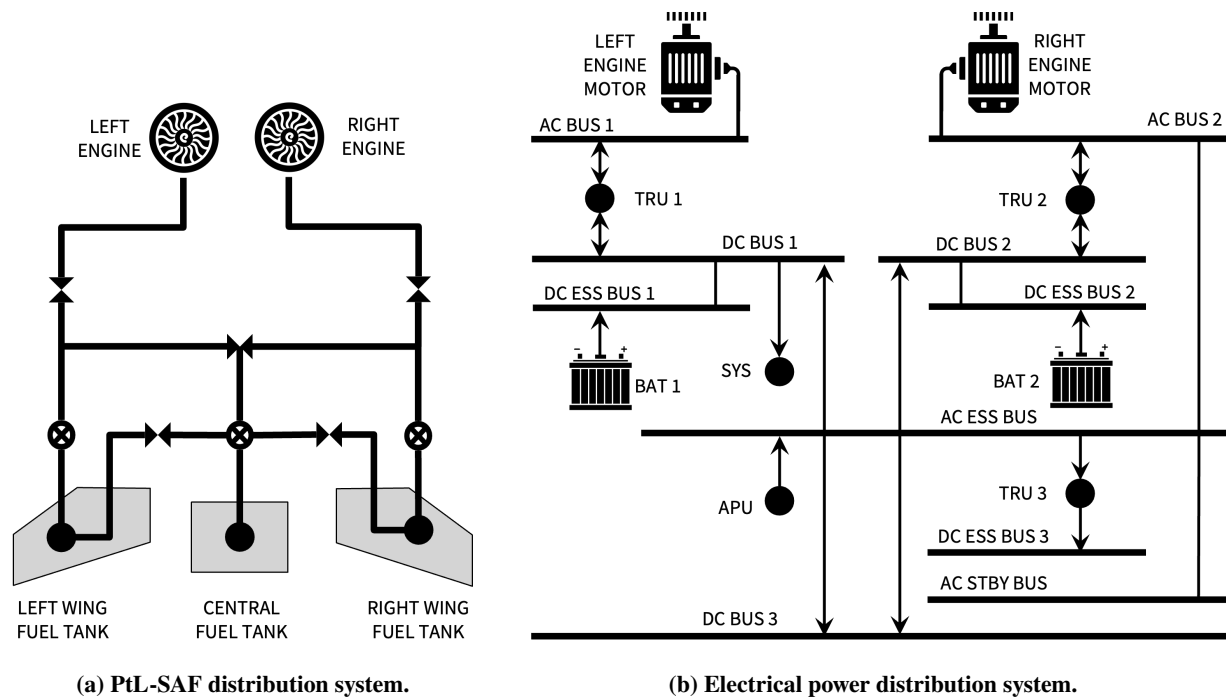


Fig. 4 Parallel hybrid network of retrofitted A220 aircraft.

In addition to Converters, the remaining functional elements play essential roles in the simulation architecture. Distributors manage the allocation of mass, energy, or power across subsystems, enabling coordinated flow within the network. Modulators regulate power flow to ensure stable and controlled system behavior under varying operating conditions. Propulsors serve as a specialized subset of converters that work in concert to generate thrust by transforming thermodynamic energy into mechanical force. Sources represent energy storage components, such as fuel tanks or batteries, and act as the origin of energy flow within the system.

To garner high resolution of emission produced from each fuel, a chemical reactor network (CRN) representation of the combustor was employed. This network is simulated in Cantera [16], an open-source toolkit for chemical kinetics, thermodynamics, and transport processes; the framework supports detailed reaction mechanism simulations within each

reactor. Cantera facilitates the calculation of species concentrations and reaction rates crucial for emissions predictions, allowing the capture of the chemical kinetics involved in combustion processes [17]. Previous studies have demonstrated the capabilities of CRNs in modeling combustion [18, 19]. Figure 5a presents a cross-sectional schematic of an RQL burner. In Fig. 5b, the general schematic of a Rich-Burn, Quick-Mix, Lean-Burn (RQL) burner and the building blocks of the combustor CRN are shown: Perfectly Stirred Reactors (PSRs) and Plug Flow Reactors (PFRs). The assembly of different PSRs and PFRs allows the creation of CRN.

The combustor CRN model is designed to simulate combustion processes and evaluate emissions by accepting a set of defined inputs and generating corresponding outputs. Key input parameters to the CRN model include combustor inlet conditions, such as temperature, pressure, and air mass flow rate, as well as the fuel-to-air ratio. The model also accounts for combustor geometry and incorporates a kinetic mechanism that governs the chemical reactions specific to the fuel type. Based on these inputs, a range of thermochemical outputs at the combustor exit, including the stagnation temperature, pressure, enthalpy, the post-combustion fuel-to-air ratio, and species masses such as CO₂, H₂O, NO_x, and CO are computed. Emission indices can then be determined using the expression below:

$$EI_i = \frac{m_i}{m_{fuel}} \quad (1)$$

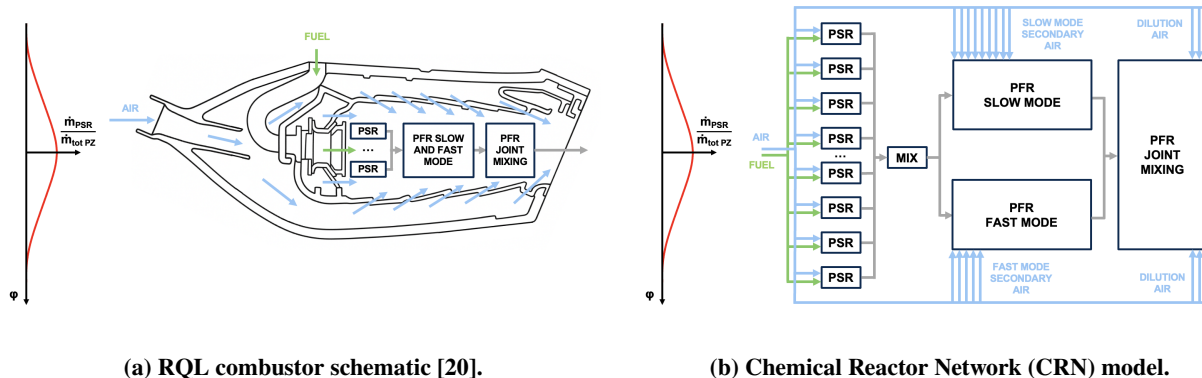


Fig. 5 RQL burner architecture and RCAIDE modeling using a chemical reactor network approach.

B. Component Modeling and Design Considerations

Lithium-Ion Battery Modules and Packs

Incorporating batteries into the wing is a critical design decision for advancing hybrid and battery-electric aircraft, providing substantial structural weight savings through bending relief [21]. Although impractical for PtL-SAF, relocating the fuel storage within the fuselage underscores the need to alleviate bending moments. Given an anticipated volume of 21 m³ outside the rotorburst zone, one may approximately calculate the cumulative capacity of all the cells arranged as individual modules positioned within the wingbox between successive ribs. The estimation of wing volume was determined using the shapely [22].

The attributes of the cylindrical 18650 lithium-ion batteries analyzed in this research were projected based on contemporary technology to a specified era. The cells weighed 48 grams, with a unit volume of around 0.05 m³ to facilitate internal module temperature management. Additionally, a packing factor of 1.1 is used for the final volume of all cells, while a weight factor of 1.42 is applied to the total weight of the battery cells to account for the battery management systems, sensors, and protective layers.

Shaft-Mounted Axial Motor

An axial flux motor is a configuration of electric motor design in which the space between the rotor and stator, and consequently the orientation of magnetic flux, is aligned parallel to the axis of rotation, in contrast to the radial alignment found in the more prevalent radial flux motor with its concentric cylindrical geometry. Axial-flux motors occupy less volume and are optimal for applications with spatial limitations, such as airplane engines. The compact

pancake configuration, along with axial-flux motors, provides a larger magnetic surface and total surface area, enabling designers to increase the capacity of thermal management systems. Furthermore, they observe that their geometry intrinsically experiences torque growth proportional to the cube of the rotor diameter, whereas in a radial flux, the increase is merely quadratic; hence, they are ideally suited for coaxial mounting on the engine shaft.

The motor for each hybrid type is dimensioned based on the power distribution it is designed to provide at top-of-climb. By utilizing the RPM and shaft power from the mission simulation of the baseline Jet-A variants, one may determine the motor's design torque. To achieve a designated efficiency, the battery electrical configuration, which determines the nominal electrical bus voltage and the no-load current, is employed to calculate the speed constant and internal resistance of the motor.

Low-Volumetric-Density and Cryogenic Alternative Fuels Storage

Table 2 summarizes the key thermophysical properties of PtL-SAF, LPG, LNG, and LH₂, including specific energy, volumetric energy density, and reference liquid density at the indicated temperature and pressure conditions. These temperatures and pressures, obtained from a literature survey of existing architectures, pose some of the biggest challenges aircraft configurators face in realizing architectures that utilize low-carbon fuels: high volumes required for energy storage coupled with low gravimetric energy densities. Here, gravimetric energy density is defined as the ratio of the weight of the liquid fuel to that of the tank and fuel system, along with the liquid fuel, and although it is not explicitly covered in this paper, it contributes in a large part to the added operating empty weight (OEW) of the aircraft. Gravimetric energy density is strongly coupled with the storage tank design, notably the material and aspect ratio, which determine the load exerted on key points of failure in the pressure vessel.

For the foreseeable future, aviation is expected to adopt mature cryogenic tank storage technology, namely, large cylindrical tanks that do not fit within the wings. While synthetic kerosenes like PtL-SAF can leverage existing tanks and wet-wing technology onboard the aircraft, the three remaining fuels will require a completely different approach with large pressurized tanks within the main fuselage and new wing designs that cleverly house batteries within the wing box to provide bending moment relief. Studies adopting orthodox, cylindrical, rounded-cap storage tanks have shown that future aircraft powered by LH₂ would see tank gravimetric energy densities between 50 and 65, while others report LNG and LPG at around 55 and 60, respectively. In this study, the more conservative value for LH₂ was opted for.

Table 2 Thermophysical properties of the fuels considered in this study.

Category	Fuel	Specific Energy [MJ/kg]	Energy Density [MJ/L]	Liquid Density [kg/m ³]	Gravimetric Storage Density [%]	Ullage Fraction [%]
Non Cryogenic	PtL-SAF	43.2	35.3	820 at 288.15 K, 1 atm	78	2
	LPG	48.0	25.3	550 at 293.15 K, 8 atm	60	20
Cryogenic	LNG	50.2	21.9	450 at 111.15 K, 1 atm	55	5
	LH ₂	119.9	8.49	70.99 at 20.35 K, 1 atm	50	7

As noted in the recently concluded Boeing CASCADE Sustainable Aviation Forum, one of the major pitfalls of research into alternative energy fuels is the lack of consideration of airframe integration, crippling a thorough review of CONOPS. Moreover, assessing the power consumption alone is not sufficient to conclude that an aircraft can even operate: a designer should consider all elements of flight, from aerodynamics, stability and control, propulsion, structural aeroelasticity, etc., when evaluating a configuration. Deviating from many prior studies, this work also encompasses a semi-quantitative assessment of energy storage and transmission integration onto the system of interest. Under the assumption that the OML is kept fixed, nine design considerations are expanded upon before scoring 10 configurations. The result of which is provided in the decision matrix (Table 3)

- 1) **Tank Gravimetric Index:** The gravimetric index is the ratio of the fuel inside a fuel tank to the entire fuel-tank system [23]. High gravimetric indices are preferable to maximize usable weight.

- 2) **Rotorburst Zone Avoidance:** A rotorburst is a failure scenario where any rotating engine component fractures at high speed. The rotorburst zone is the necessary volume around the engine where no critical systems, like fuel lines or tanks, are in the path and at risk of being struck by turbine blades [24].
- 3) **Nominal Boarding/Deplaning:** The flow of passengers entering and exiting the plane imposes constraints on fuel tank locations, especially when tanks must be located near cabin areas. Large fuselage-mounted tanks (often in the case of cryogenic fuel sources) must not obstruct aisles, interfere with emergency exit pathways, or inhibit the turnaround process.
- 4) **Emergency Egress:** As per FAA requirements, all aircraft with more than 44 passengers must have an emergency evacuation time of 90 seconds when using 50% of the exits [25]. Any tank placements, especially near exits, must ensure that evacuation paths remain clear and structurally sound.
- 5) **Preservation of Cargo Space:** Lower energy-density fuels require larger tank volumes, which can encroach on belly-cargo volume. The loss of this space can reduce cargo revenue and undermine the economic feasibility of alternative fuel architectures.
- 6) **Gear Retracted Emergency Landing:** FAR and EASA regulations require aircraft to be designed so that the fuel system will not rupture and leak enough fuel to create a fire hazard during a wheels-up landing. This applies to minor crash scenarios, including those in which the landing gear is fully or partially retracted. [26].
- 7) **Weight and Balance:** Large fuel-storage systems, especially those that are fuselage-mounted, can shift the center of gravity forward or aft during flight, adding further strain on the stabilizer. Placing tanks close to the aerodynamic center or distributing the mass symmetrically about the center of gravity tends to result in better-performing aircraft.
- 8) **Volume Availability:** The volume required to store alternative fuels, especially LH₂, is substantially larger due to lower energy densities [27]. With a fixed outer mold line, only some areas of the aircraft provide adequate room for the tanks, each of which comes with its own structural and operational trade-offs, some of which are discussed in this list.
- 9) **Emergency Fuel Venting and Fuel Jettison:** Since many of the alternative fuels studied in this paper are stored in cryogenic or pressurized tanks, extra considerations have to be made when dumping these fuels in an emergency. Because liquid nitrogen, liquid petroleum, and liquid hydrogen have such low boiling points and high vapor pressures [28], architectures must support pressurization and prevent flash-freezing of vapor around the nozzle exit so that fuel can be safely jettisoned.

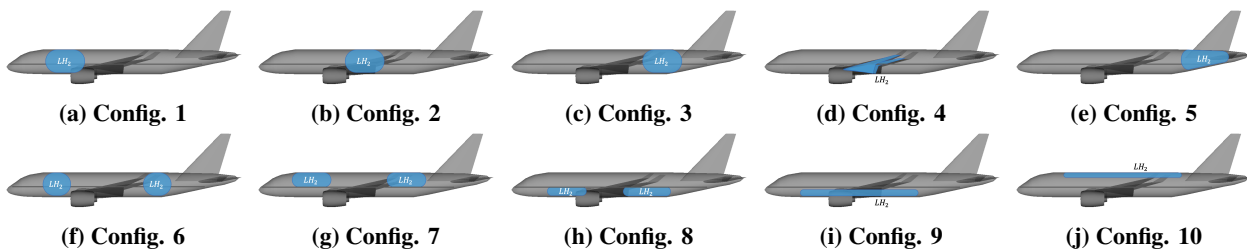


Fig. 6 Candidate configurations for low-volumetric density alternative fuels: (a) Forward-positioned tank spanning cabin and cargo bay; (b) Center-positioned tank spanning cabin and cargo bay; (c) Aft-positioned tank spanning cabin and cargo bay; (d) Wing-integrated tank; (e) Empennage tank; (f) Forward and aft tank (g) Forward and aft tank spanning cabin only; (h) Forward and aft tank spanning cargo bay only; (i) Elongated tank spanning cargo bays/wingbox; (j) Elongated tank spanning top of cabin.

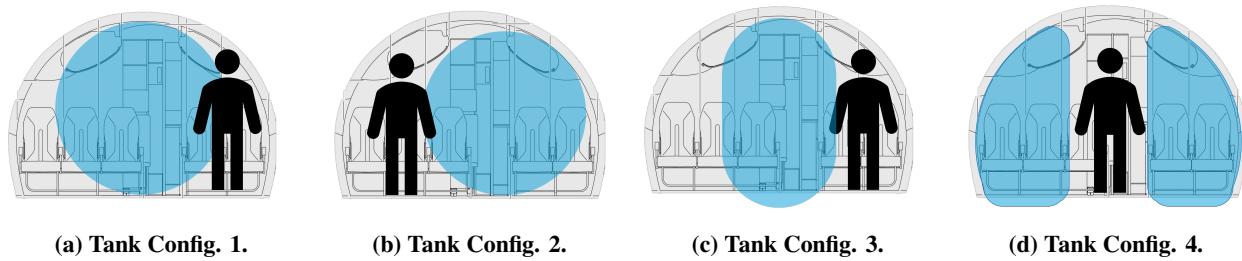
Each aircraft configuration enumerated above possessed distinct advantages and disadvantages. Tanks with a higher aspect ratio tend to require greater structural support and material thickness to withstand the stresses from membrane and bending loads, and therefore exhibit lower gravimetric indices. Consequently, combinations (d), (g), and (h) received lower scores. Furthermore, as these heavy tanks are non-conformal, orientation and spatial constraints will affect the aircraft's stability. Tanks that failed to properly distribute weight to sustain a static margin akin to the baseline aircraft incurred significant deductions in feasibility points as well. Third, tanks located within the rotor-burst zones of the turbofan engine, particularly those extending along the fuselage or centrally located, faced substantial penalties. Many proposed animation layouts surprisingly neglect to account for passenger boarding and egress, both under typical and emergency scenarios. These accounted for in the third and fourth tank placement design considerations, and the scores within Table 3 reflect these sentiments. Furthermore, considering cargo space is essential for developing a feasible idea.

Table 3 Decision matrix for configurations 1-10. Scores range from 1 (red, worst) to 10 (green, best).

Criterion \ Configuration	1	2	3	4	5	6	7	8	9	10
Tank Gravimetric Index	7	7	7	2	5	6	6	6	4	4
Rotorburst Zone Avoidance	10	9	10	3	10	10	10	7	1	1
Nominal Boarding/Deplaning	6	6	6	10	10	5	5	10	10	7
Emergency Egress	3	3	3	7	7	2	2	7	7	4
Preservation of Cargo Space	7	8	7	10	10	6	6	2	1	4
Gear Retracted Emergency Landing	3	3	3	8	4	2	9	1	1	10
Weight and Balance	2	7	2	5	1	7	7	6	6	6
Volume Availability	10	10	10	3	5	10	10	5	6	2
Emergency Fuel Venting and Jettison	9	9	9	7	8	7	7	2	9	9
Average Score	6.4	6.8	6.3	6	6.6	6.1	6.9	5.1	5	5.2

The tank assemblies that failed to consider this were consequently rated poorly. Lastly, while it is still unclear whether venting of gaseous cryogenic fuel from boil-off will be permissible at the airport, it is a safe practice for LH₂ systems for today. To account for this possibility, tanks that have clear means of depressurization and gas release upward are weighted higher.

Ultimately, configuration seven emerged as the highest score. It, however, needed further refinement, since there are many ways to fit such a large cryogenic tank within the aircraft's cabin. A subsequent, smaller trade study was therefore undertaken. In it, the four arrangements depicted in Figure 7 were assessed using the selection criteria listed in Table 4. While having one large cylindrical tank within the center of the aircraft would result in the largest cross-sectional diameters, it would severely impact passenger traffic. Moreover, since the aircraft is of the extra-narrow-body class, there would not be sufficient vertical clearance for the upper torso and head of adult passengers. Out of this second trade, tank configuration three emerged as the frontrunner in the design space exploration. Although a detailed structural analysis is not undertaken here, the existence of literature points to the conclusion that rounded vertical endcaps with a slender side provided sufficient room for passengers to exit the aircraft via both forward and aft doors in the event of an emergency.

**Fig. 7 Tank placement configurations within the A220-100 fuselage.**

Tank sizing was based on an initial determination of the energy required for a nominal mission of conventionally fueled aircraft. This energy was converted to volume using the specific energies and densities of the fuels considered within this study. Based on the ullage fractions listed in Table 2, the gross volume of the tank can be computed first. Note that for low-volumetric-density fuels, it is a safe assumption that for payload range analyses (not discussed here), this computed volume for the design range is close to the maximum fuel volume of the aircraft.

$$V_{gross} = \frac{V_{fuel}}{(1+u)} \quad (2)$$

Referencing Fig. 8 below, the volume of one elongated ellipsoid tank is given by:

Table 4 Decision matrix for tank configurations 1-4. Scores range from 1 (red, worst) to 10 (green, best).

Criterion \ Configuration	1	2	3	4
Tank Gravimetric Index	8	8	7	5
Emergency Egress	2	3	7	8
Nominal Boarding/Deplaning	2	3	7	8
Flight Stability Penalty	8	3	8	7
Volume Availability	9	9	8	6
Average Score	5.8	5.2	7.4	6.8

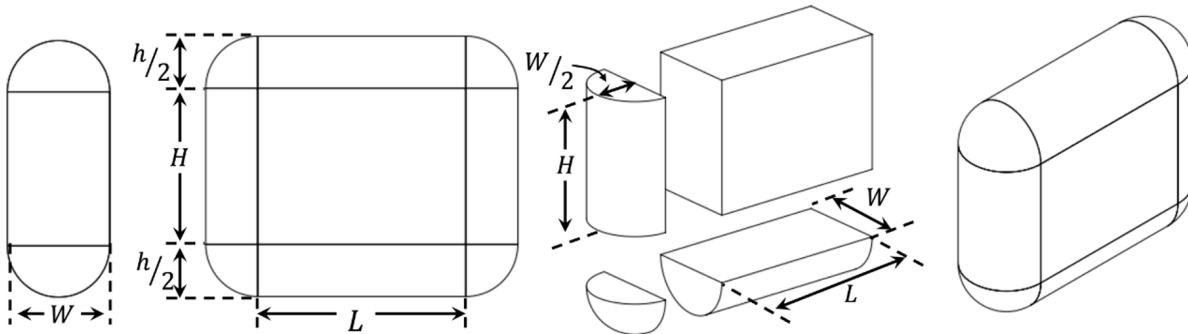


Fig. 8 Flattened cylindrical tank dimensions.

$$V_{tank} = V_{top/bottom\ end\ caps} + V_{front/back\ end\ caps} + V_{center\ body} + V_{corner\ caps} \quad (3a)$$

$$V_{tank} = \frac{\pi WLh}{4} + \frac{\pi WHh}{4} + LWH + \frac{\pi h^2 W}{6} \quad (3b)$$

Using a factor to relate the cumulative length of the forward (f) and aft (a) tanks to each respective tank as shown below:

$$L_{f+a} = L_a + L_f \quad (4a)$$

$$L_a = (1 - \alpha)L_{f+a} \quad (4b)$$

$$L_f = \alpha L_{f+a} \quad (4c)$$

$$(4d)$$

one can rearrange to solve for L_{f+a}

$$L_{f+a} = \frac{V_{tank} - \left(\frac{\pi WHh}{2}\right) + \left(\frac{\pi h^2 W}{3}\right)}{\left(WH + \frac{\pi hW}{4}\right)} \quad (5)$$

IV. Hybrid Powertrain Modeling

A. Sizing and Integration Approach

The hybrid-electric propulsion architecture developed for this study is implemented within the RCAIDE simulation framework and couples a conventional turbofan propulsion system with electrically driven low-pressure compressors and dual wing-mounted battery packs. For each Latin Hypercube sample, the baseline Airbus A220-100 configuration is instantiated, and its propulsion network is replaced by a hybrid-electric network whose sizing is governed by two key parameters: the hybrid power split ratio, which allocates a fraction of LPC power to electric motors, and the number of parallel battery strings, which determines the total electrical energy and peak power available. A Latin Hypercube Sampling strategy is employed to explore this design space efficiently.

For each sample, the hybrid network is constructed by clearing the default propulsion definition and creating a hybrid powertrain that includes an electrical bus with two lithium-ion NMC battery modules. Each module contains a fixed number of cells in series and a variable number of parallel strings. The battery modules are co-located at the wing center of gravity to maintain a favorable mass distribution. Electric motors are attached to the LPC shafts of both turbofan engines, and each motor is sized, determining the design torque, current, voltage, and operating speed. The turbofans retain their nominal cycle parameters, but their LPC behavior is modified to reflect the electric assistance. Once the network is defined, a preliminary mission evaluation provides the required fuel mass, serving as the basis for subsequent tank sizing and constraint reconciliation steps.

Battery sizing is performed using a geometric cell model with packaging and BMS overhead factors. Additional mass contributions from the electric motors, inverters, and cabling are computed with empirical relationships based on torque and current requirements. Each resulting hybrid design point is therefore fully mass-closed and physically consistent before evaluating its final mission performance.

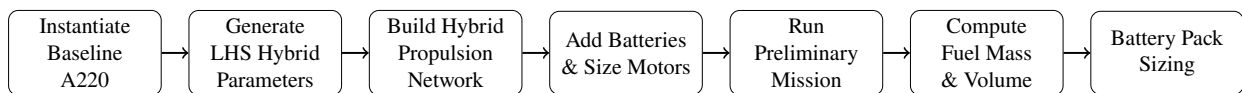


Fig. 9 Flowchart of hybrid-electric powertrain sizing and integration.

B. Aircraft Component Weight and Volume Constraint Reconciliation

The first step of this phase is the integration of fuselage-mounted fuel tanks. The mission-derived fuel mass is converted into a required fuel volume using the density and ullage fraction of the selected fuel, and two non-integral fuselage tanks are created and positioned within the cabin footprint. Their combined geometry displaces a portion of the cabin, reducing the cabin length and therefore the available passenger seating volume. To determine the resulting passenger capacity, two cubic spline surrogate models are generated prior to the sweep. One maps cabin length to the number of seat rows, and the other maps cabin length to the total number of passengers.

The overall aircraft mass is then updated. The fuel-system mass is recomputed to reflect the new tank architecture. The operating empty weight is then increased by the battery mass, the electric motor mass, the inverter mass, and the wiring mass. These updates produce a revised operating empty weight. The allowable payload is determined and the number of passengers allowed by mass is then compared to the number allowed by volume, and the lesser value is taken as the feasible passenger capacity. Once a feasible configuration is identified, meaning both mass and volume constraints are satisfied, a second mission evaluation is performed to compute the final performance metrics.

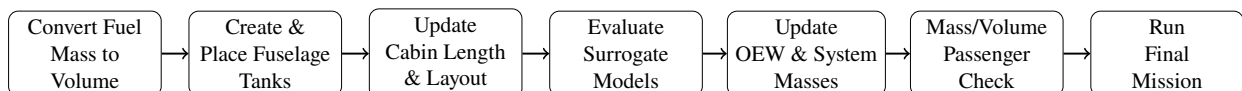


Fig. 10 Flowchart of aircraft component weight and volume constraint reconciliation.

V. Design Space Exploration

A. Latin Hypercube Sampling

To explore the coupled design space of hybridization strategies, onboard energy storage, and alternative fuels, a Latin Hypercube Sampling (LHS) methodology was employed. LHS is a stratified sampling technique that generates quasi-random samples with improved space-filling properties compared to purely random or grid-based sampling. Unlike full-factorial sweeps, which become computationally intractable as dimensionality grows, LHS ensures that each design variable is sampled uniformly across its range while requiring significantly fewer total evaluations. In this study, LHS is defined over a seven-dimensional design vector comprising the hybridization fractions applied across the mission and the number of parallel-connected battery modules:

$$\mathbf{x} = [\phi_1, \phi_2, \phi_3, \phi_4, \phi_5, \phi_6, n_{\text{parallel}}]^T.$$

Each hybridization parameter ϕ_i represents the fraction of turbine shaft power replaced with electrical power during mission segment i . The six segments used in this work are listed in Table 5.

Table 5 Mission segments corresponding to hybridization parameters ϕ_i .

Parameter	Flight Regime	Mission Segments
ϕ_1	Takeoff	Ground Acceleration; Takeoff Roll
ϕ_2	Low-altitude climb	Initial Climb, Climb to FL 50
ϕ_3	High-altitude climb	Climb to FL 100; Accel.to Climb Speed; Climb to FL 300
ϕ_4	Cruise	Constant Speed Cruise
ϕ_5	Descent	Descent to FL 300; Final Descent
ϕ_6	Landing	Approach; Landing

Initial scoping studies showed that moderate or high hybridization levels would require battery masses and volumes incompatible with the A220-100 airframe. Therefore, only mild-hybrid retrofit configurations were considered feasible. This is reflected in the hybridization bounds:

$$\phi_i \in [0, 0.125], \quad i = 1, \dots, 6,$$

which limit electrical augmentation to 12.5% of shaft power in any mission phase. The seventh dimension, n_{parallel} , specifies the number of battery modules connected in parallel. This discrete parameter governs pack voltage, current capability, power limits, and total stored energy. To span the full feasible range while respecting geometric and mass constraints of the A220-100, the following bounds were selected:

$$n_{\text{parallel}} \in [0, 1500].$$

Together, these bounds define a feasible region for mild parallel-hybrid architectures using each of the four candidate fuels examined in this study: PtL-SAF, LPG, LNG, and LH₂. A Latin Hypercube with dimensionality $d = 7$ was constructed for each fuel type. For every fuel,

$$N_{\text{samples}} = 2000,$$

yielding a total of 8000 full mission simulations across all fuels. Each sample corresponds to a unique hybridization schedule and battery configuration, followed by a complete evaluation of the propulsion system, mission performance, emissions, fuel-tank resizing, cabin-layout (LOPA) constraints, and weight-and-balance effects. This approach enables a statistically representative exploration of the design space while preserving computational tractability.

B. Monte Carlo Uncertainty Quantification

To quantify the sensitivity of the combustor's chemical-kinetic and mixing predictions to parameter uncertainty, a Monte Carlo Uncertainty Quantification analysis was performed. This methodology propagates uncertainty by repeatedly

sampling the input space and evaluating the model response. The resulting output captures the statistical variability of the system without imposing assumptions of linearity or Gaussian behavior. The combustor model contains eleven geometric, mixing, and equivalence-ratio parameters, collected in the vector \mathbf{p} :

$$\mathbf{p} = [V, L, L_{PZ}, S_{PZ}, \phi_{PZ}, \phi_{SZ}, f_{SM}, \ell_{SA,SM}, \ell_{SA,FM}, \ell_{DA,start}, f_{mix}]^T,$$

where ϕ_{PZ} and ϕ_{SZ} denote the design equivalence ratios in the Primary and Secondary Zones, respectively. Nominal values are then defined and each parameter is assigned an uncertainty interval of $\pm 5\%$ around its nominal value:

$$p_i \sim \mathcal{U}(0.95 p_{i,0}, 1.05 p_{i,0}).$$

Uniform random samples are then generated using:

$$X = \{\mathbf{p}^{(1)}, \dots, \mathbf{p}^{(N)}\}, \quad N = 500,$$

where each row of X represents one realization of the input vector. For each sample, the combustor configuration is reconstructed and passed to the CRN solver. The Monte Carlo propagation function runs all N samples and returns the resulting set of structured outputs:

$$Y = \{\mathcal{Y}^{(1)}, \dots, \mathcal{Y}^{(N)}\},$$

where each $\mathcal{Y}^{(i)}$ contains the temperatures, species mass fractions, reaction rates, and emissions indices produced by the CRN solver. For every output element, the distribution across valid samples is used to compute mean, standard deviation, $q_{0.05}$, median and $q_{0.95}$.

VI. Baseline Aircraft Validation

A. Weight Estimation

Although there is less available weight breakdown information for the A220-100, the team was still able to validate key elements against empirical data of operating empty weight, engine weight, and nominal C.G. location. For the weight breakdown, the NASA FLOPS estimation methodology was used [29]. This method uses aircraft geometry and key vehicle-level properties, such as maximum takeoff weight and number of passengers, to estimate total aircraft weight and component weights. The estimated operating empty weight, was 35404 kg a 0.52% difference from the APM's 35221 kg. The weight breakdown for the A220 is shown in Figure 11 where the percentages of the maximum zero fuel weight are shown. The total MZFW is 48982.70 kg.

B. Performance

Payload range results were compared to the nominal diagram presented in the APM. Validating the payload range serves to help validate the coupled propulsion and aerodynamics systems. In Figure 12a, The fuel reserve percentage was set at 10% of the total fuel in order to meet the given requirements. As seen in the graph, the slopes of the maximum takeoff weight line closely agree with the APM payload range which strongly supports the coupled propulsion and aerodynamic modeling.

Performance results were also validated by comparing thrust specific fuel consumption and fuel flow rate as seen in Figure 12d and Figure 12c. These values were obtained with the flight profile shown in Figure 3. The SFC corresponds to about a 10% decrease from the CFM56 which is an often specified comparison point for the PW1500G engines on the A220 [30].

C. Turnaround Time

The turnaround time graph was also based on the nominal chart shown in the APM, which assumed 94 passengers on board, a passenger boarding rate of 18 per minute per door, and a passenger deplaning rate of 12 per minute per door. A two-door configuration was assumed for both boarding and deplaning, which allows these processes to occur in parallel and reduces the overall passenger-related contribution to turnaround time. The aircraft is also equipped with a forward and aft compartment for luggage storage, which are loaded and unloaded simultaneously. Furthermore, ground servicing tasks such as catering, cabin cleaning, and routine inspections were assumed to follow standard times for a narrow body aircraft and were not treated as limiting factors unless they intersected with passenger or refueling operations.

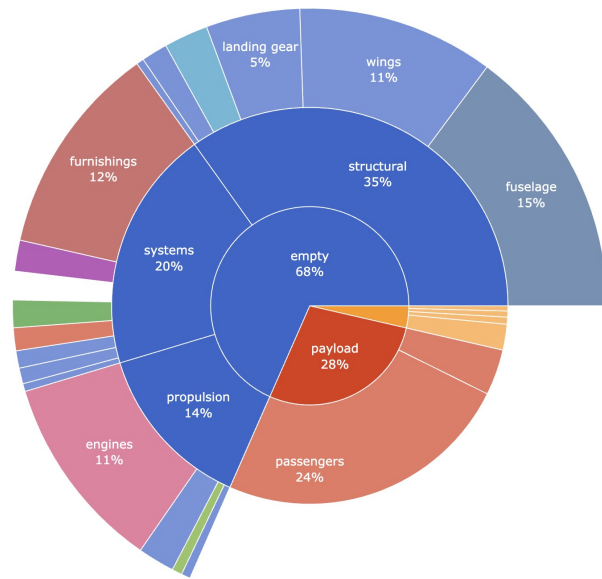
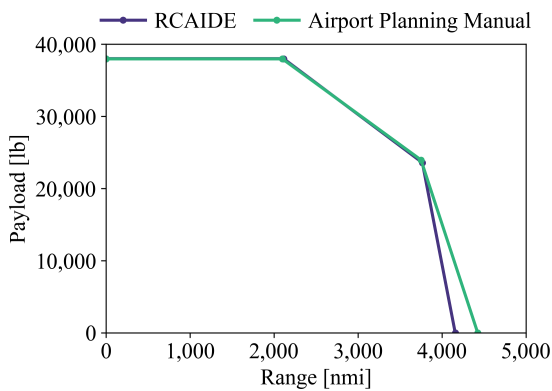
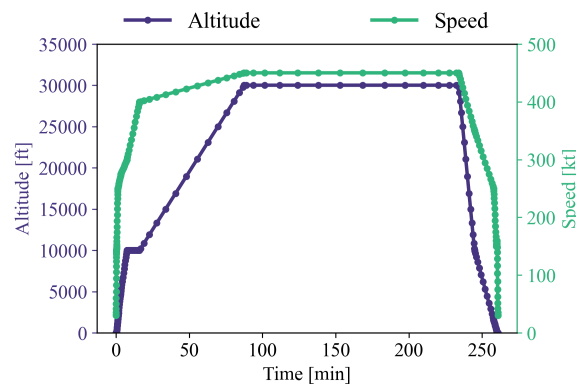


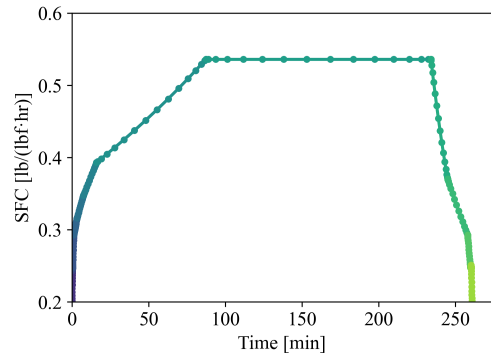
Fig. 11 A220-100 RCAIDE weight breakdown percentages.



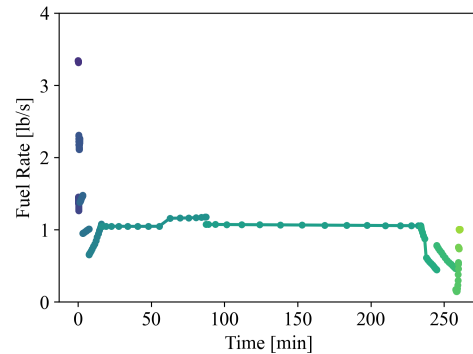
(a) Payload-range diagram.



(b) Altitude and airspeed.



(c) Specific fuel consumption.



(d) Fuel flow rate.

Fig. 12 Conventional A220-100 RCAIDE fuel consumption and payload-range validation.

Refueling operations were assumed to occur either through a center tank or two wing tanks, with a nominal refueling rate of 140 gallons per minute. Alternative fuels were also considered, with their refueling rates being scaled by their respective densities. As a result, plots with LNG, LPG, and LH₂ show a longer turnaround time. In addition, battery recharging associated with the hybrid powertrain is also included in the turnaround analysis. Both fuel type and hybridization factor were varied throughout missions, resulting in various plots. Figure 13 shows the turnaround time operations using Jet A onboard a conventional configuration.

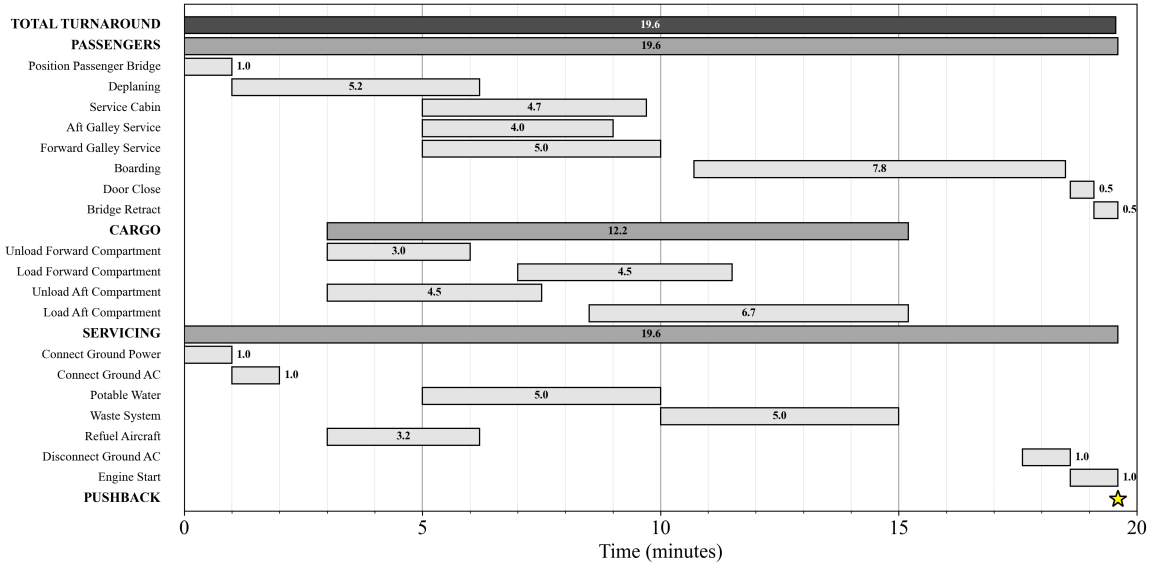


Fig. 13 Turnaround Time.

VII. Results

A. Aircraft Retrofit Comparative Analysis

A Latin hypercube sampling (LHS) approach was employed to explore a wide range of design combinations involving the hybrid power split ratio and the number of battery cells connected in parallel. Through this process, multiple variants of a mild parallel-hybrid electric Airbus A220-100 were synthesized and evaluated. For each configuration, key performance metrics were computed, particularly the energy consumption per revenue passenger kilometer (RPK) and the cost per revenue passenger kilometer. The cost of electricity was assumed to be \$0.20/kWh, while the fuel prices adopted in this study are summarized in Table 6. These values were selected based on publicly available sources representative of current or near-term market conditions.

The resulting design space was subsequently filtered to retain only configurations for which the final battery state of charge remained positive, thereby excluding cases in which the battery was undersized and unable to supply the required mission energy. From this filtered set, the configuration minimizing the total cost per revenue passenger kilometer was identified for each fuel type, and the corresponding performance metrics were extracted.

Table 6 Assumed cost per gallon for each fuel type used in the cost-per-RPK analysis, with corresponding data sources.

Fuel Type	Cost per Gallon [\$/gal]	Reference
PtL-SAF	9.00	[31]
LPG	2.50	[32]
LNG	2.70	[32]
LH ₂	1.61	[33]

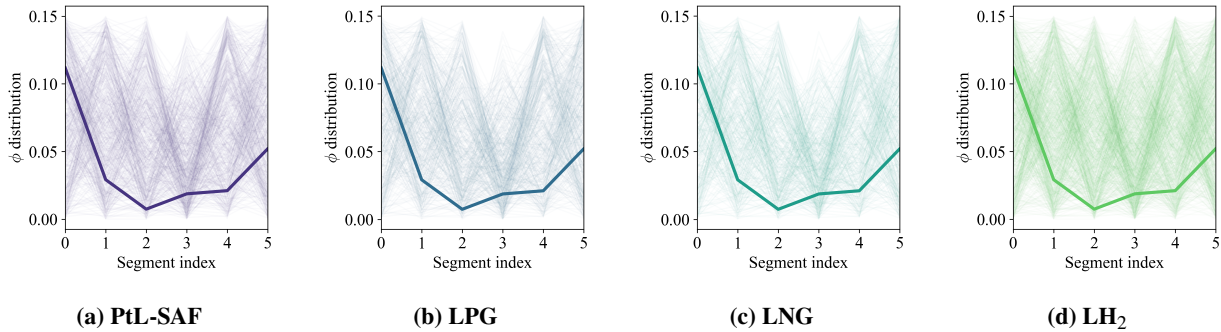


Fig. 14 Optimal segment-wise hybridization ratio ϕ for each fuel type. Each subplot shows all feasible trajectories and the best-performing configuration.

Interestingly, all four fuel-specific aircraft variants converged to the same optimal hybridization profile along the mission, as illustrated in Fig. 14. In particular, the results indicate elevated hybridization factors during mission phases characterized by high thrust demand, namely ground acceleration and takeoff, as well as during the approach and landing segments. Conversely, during the central cruise phase, the hybridization factor is progressively reduced.

This behavior is consistent with the performance characteristics of gas turbine engines, which typically exhibit higher specific fuel consumption at high thrust settings and lower efficiency during transient operating conditions. In contrast, during cruise, the engine operates closer to its optimal efficiency point, with lower specific fuel consumption and reduced benefit from electric power augmentation. Consequently, the hybrid-electric system provides the greatest benefit during high-power, low-efficiency segments of the mission, while its contribution diminishes during cruise.

The corresponding results in terms of cost per revenue passenger kilometer are illustrated in Fig. 15, where the total cost is decomposed into its electrical and fuel-related contributions. The distribution of the LHS samples is also shown in each contour plot, highlighting the range of achievable cost-per-RPK values across the explored design space. A progressively higher density of samples is observed near the lower end of the total cost-per-RPK spectrum, indicating that the selected input parameter ranges are well suited to capture economically competitive configurations. For each fuel, the configuration minimizing the total cost per RPK is explicitly highlighted by a yellow marker. This optimal hybrid configuration is compared against the corresponding single-fuel baseline case, in which no hybridization is applied and only the alternative fuel is integrated; the latter is indicated by a red marker.

Across all fuels, the electrical cost contribution remains significantly lower than the fuel-related cost component, reflecting the mild nature of the hybridization strategy considered in this study. As a result, variations in total cost per RPK are primarily driven by changes in fuel consumption, with the electric power contribution providing only a secondary effect.

A quantitative comparison between the single-fuel baseline and the optimal hybrid configuration for each fuel is presented in Table 7. Among the four fuels considered, the most economically viable option is LPG, followed by LNG and PtL-SAF, while the liquid hydrogen configuration exhibits the highest cost per RPK under the assumed conditions. The results further indicate that, for PtL-SAF, LPG, and LNG, the introduction of mild hybridization leads to a small increase in cost per RPK, on the order of 1-2%. In contrast, the liquid hydrogen case shows a modest reduction in cost per RPK of approximately 2.5%, suggesting that hybrid-electric operation can provide a limited economic benefit when combined with hydrogen propulsion.

B. Emissions

Accurate prediction of combustor emissions is essential when comparing alternative fuels and evaluating their system-level implications for hybrid-electric propulsion. In this work, emissions are computed using a medium-fidelity CRN model, representing staged combustion in a modern RQL architecture [34]. To quantify how modeling and operating uncertainties influence these predictions, a Monte Carlo uncertainty quantification framework is applied. This enables probabilistic evaluation of key combustor outputs, namely the emission indices for CO_2 , CO , H_2O , and NO_x , as well as the combustor exit temperature, for all fuels considered.

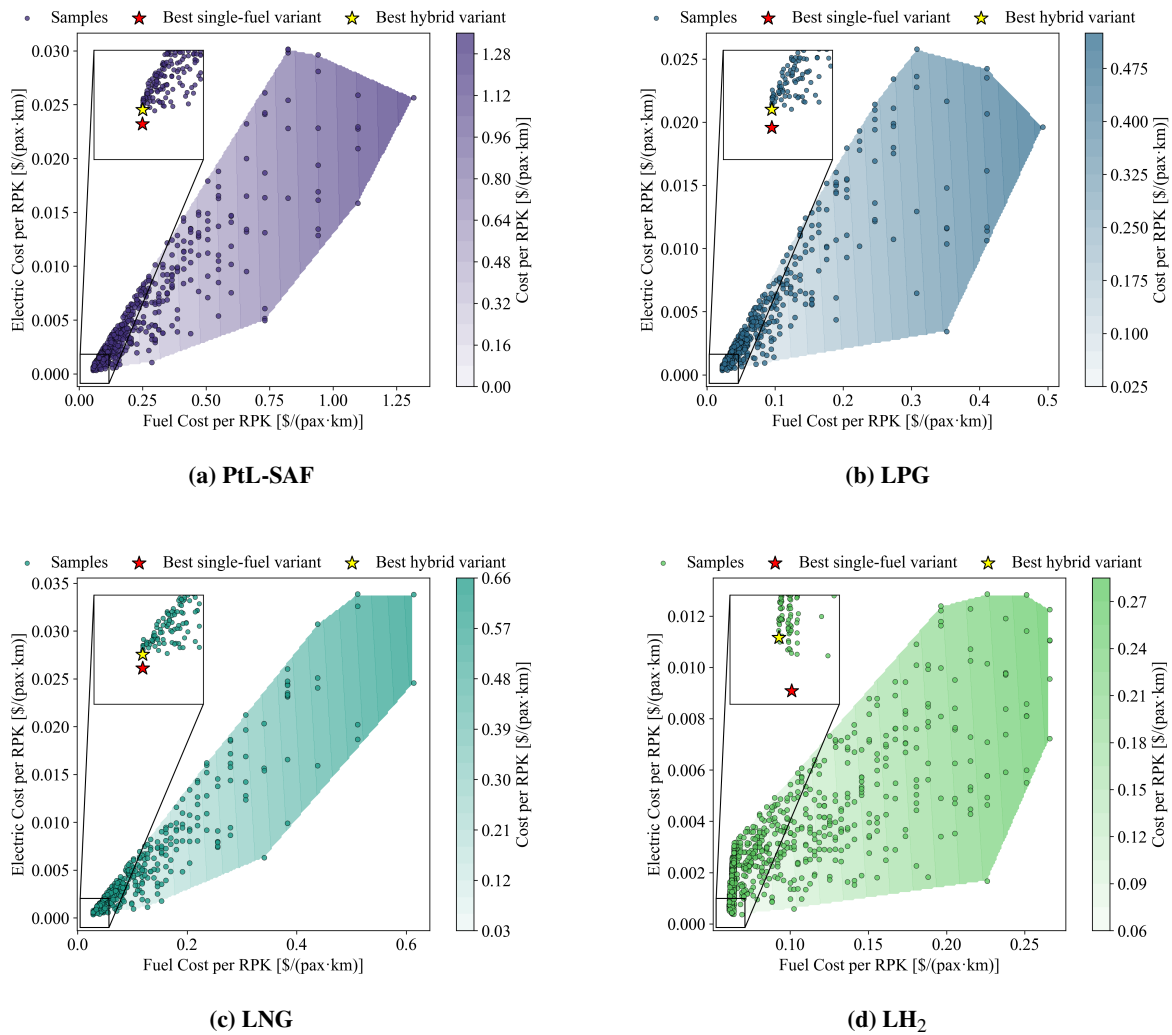


Fig. 15 Cost design-space for each fuel type.

Table 7 Cost per revenue passenger-kilometer for single-fuel baseline and best hybrid configurations, including percentage variation.

Fuel Type	Single-Fuel Baseline	Best Hybrid Case	Variation
	[\$/pax · km]	[\$/pax · km]	[%]
PtL-SAF	0.0540	0.0547	+1.30
LPG (Liquid Petroleum Gas)	0.0225	0.0229	+1.96
LNG (Liquid Natural Gas)	0.0280	0.0285	+1.49
LH ₂ (Liquid Hydrogen)	0.0631	0.0615	-2.53

1. Combustor Uncertainty Quantification and Sensitivity Analysis

Across the fuels, the histograms in Fig. 16 illustrate the distributions of Monte Carlo realizations for each emission index and for the combustor exit temperature. The CO₂ and H₂O distributions reflect the intrinsic hydrogen-to-carbon ratio of each fuel: LH₂ samples collapse to near-zero CO₂ emissions, while PtL-SAF exhibits the highest CO₂ values, with LPG and LNG occupying intermediate ranges.

For CO, the hydrocarbon fuels display broader distributions, indicating greater sensitivity to the perturbed operating

and modeling parameters. The NO_x histograms reveal distinct fuel-dependent clusters, with the LH_2 case shifted toward higher values and exhibiting increased variability relative to LPG, LNG, and PtL-SAF.

Finally, the combustor exit temperature distributions show that the LH_2 configuration attains both the highest mean temperature and the widest spread, whereas LPG and LNG results are concentrated around lower temperatures with comparatively narrower variability.

To determine which uncertain parameters most strongly influence the predicted emissions, Pearson correlation coefficients are computed between input perturbations and output responses for each fuel. The tornado plots in Fig. 17 summarize these relationships and highlight the dominant sensitivities.

The CO_2 emission index is primarily governed by the fuel carbon content and by the overall equivalence ratio. As a

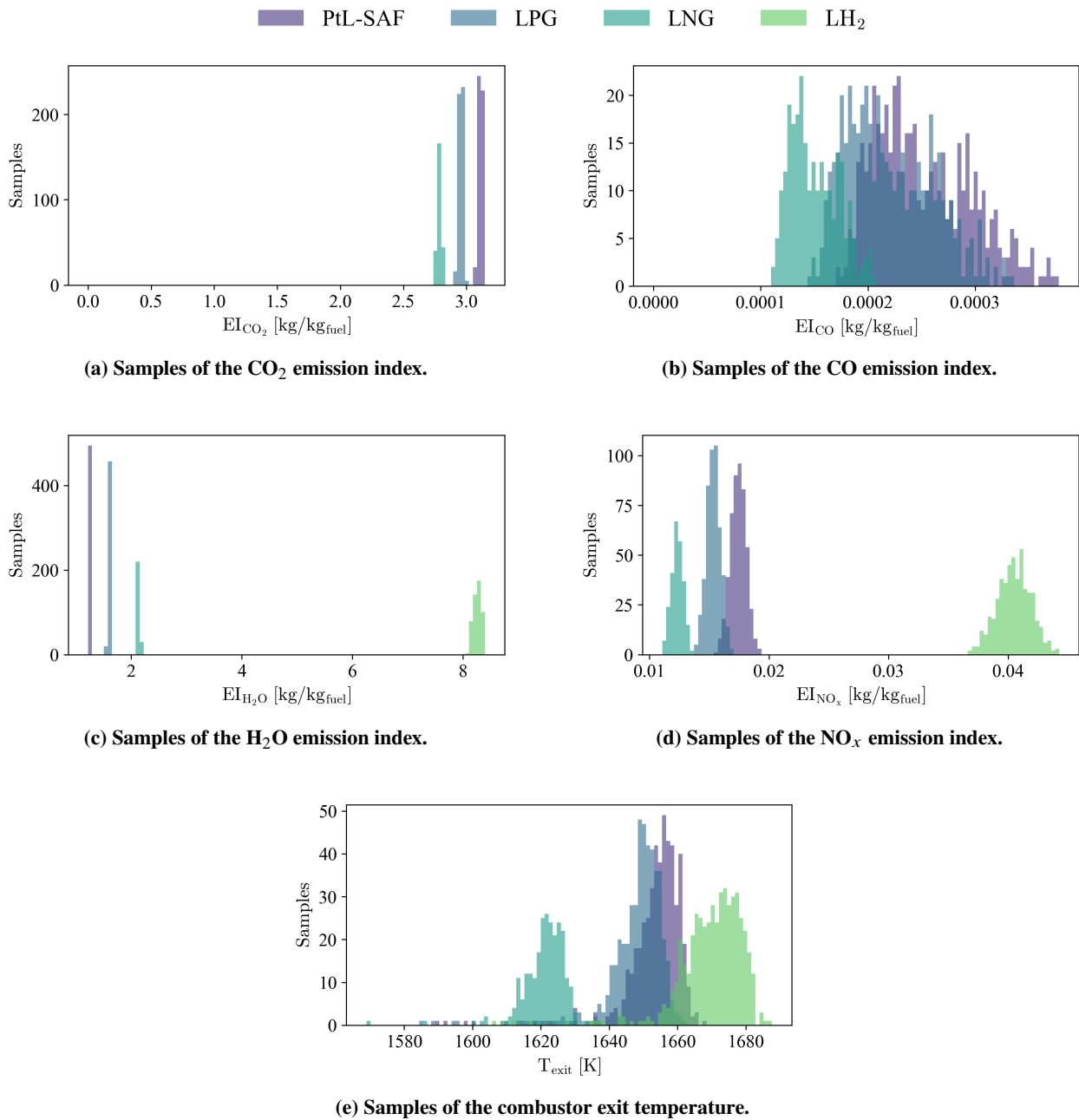


Fig. 16 Distributions of samples for the emission indices and combustor exit temperature.

result, PtL-SAF shows the strongest positive correlation between S_{PZ} and EI_{CO_2} and between $\phi_{des,PZ}$ and EI_{CO_2} , while LPG and LNG display intermediate sensitivity. As expected, LH_2 exhibits negligible correlation for EI_{CO_2} . For the CO emission index, positive correlations with $\phi_{des,PZ}$ and $\phi_{des,SZ}$ are observed for all fuels. This effect is strongest for PtL-SAF, LPG, and LNG, reflecting the sensitivity of hydrocarbon oxidation pathways to local equivalence ratio and mixing non-uniformity. In contrast, LH_2 exhibits a weaker dependence on mixing-related parameters for CO, consistent with the absence of carbon-bound species in the fuel. For the H_2O emission index, correlations are dominated by the equivalence ratio and fuel composition. LH_2 shows a strong dependence on SPZ and $\phi_{des,PZ}$, since water vapor is the primary combustion product, whereas hydrocarbon fuels exhibit weaker sensitivity. The NO_x emission index displays the strongest correlations with $\phi_{des,PZ}$. This effect is particularly pronounced for LPG. The combustor exit temperature, T_{exit} , is most strongly correlated with SPZ and the dilution-air start location $l_{DA,start}$, exhibiting a negative correlation.

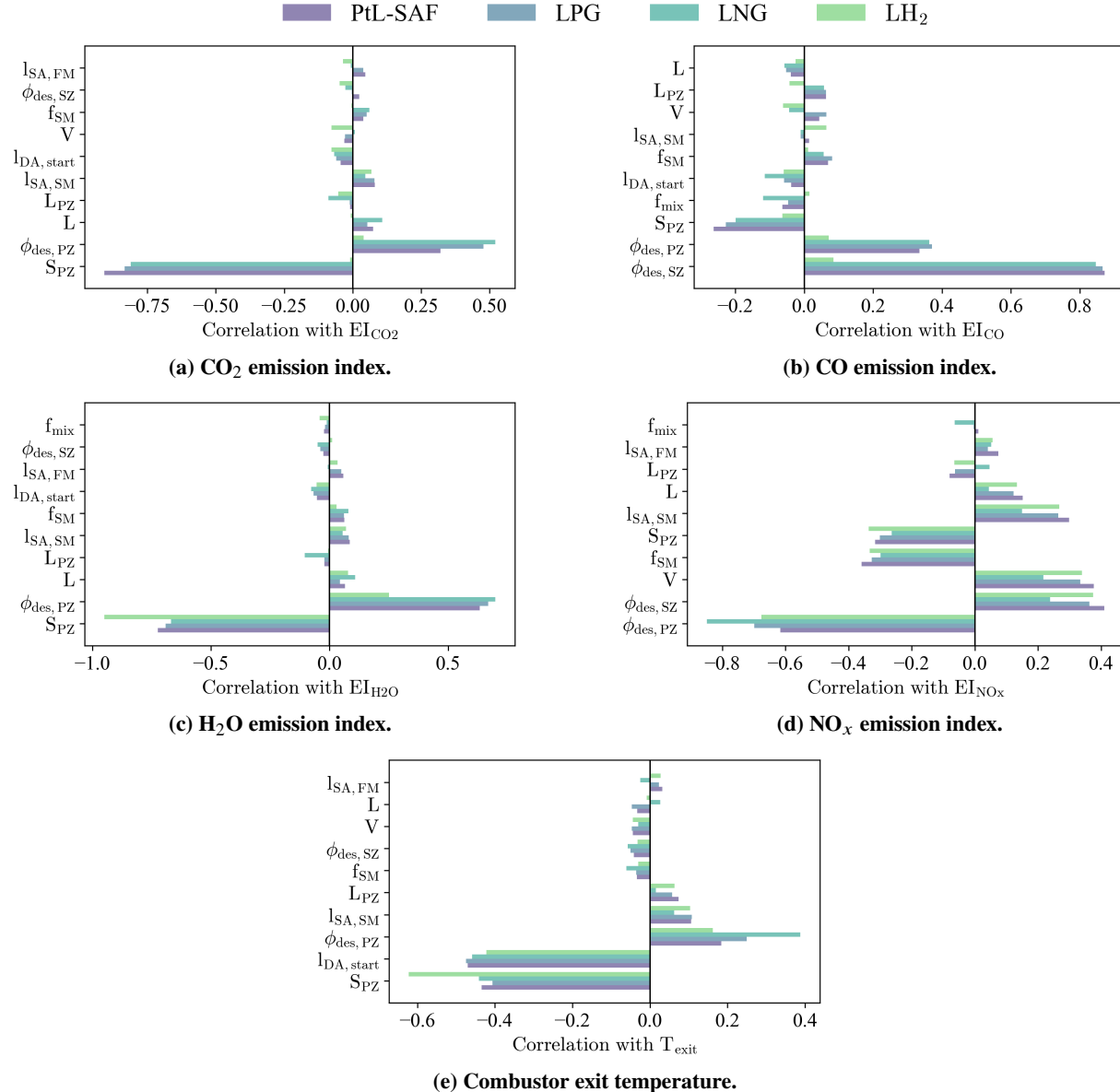


Fig. 17 Correlation-based tornado plots showing the Pearson correlation coefficients between uncertain combustor input parameters and the emission indices and combustor exit temperature for all fuels.

The thermo-chemical response across the combustor is further illustrated using band plots for the primary and secondary zones (Figs. 18 and 19), which show the mean predictions together with the associated uncertainty envelopes

for the emission indices and temperature. In all cases, the uncertainty bands remain relatively narrow and exhibit only modest deviations from the mean trends, indicating a limited sensitivity of the predicted thermo-chemical quantities to the imposed parameter perturbations.

A quantitative summary of the resulting uncertainty at the combustor exit is provided in Table 8. For the hydrocarbon fuels, the standard deviations of the CO_2 and H_2O emission indices remain below 1% of their respective mean values. Similarly, the CO emission index exhibits moderate relative uncertainty. The NO_x emission index shows variability, particularly for the LH_2 case. Nevertheless, the relative uncertainty in EI_{NO_x} remains limited, indicating a valid prediction of the trends across the explored design space. Finally, the combustor exit temperature values confirm that the overall thermal state of the combustor is weakly affected by the considered uncertainties.

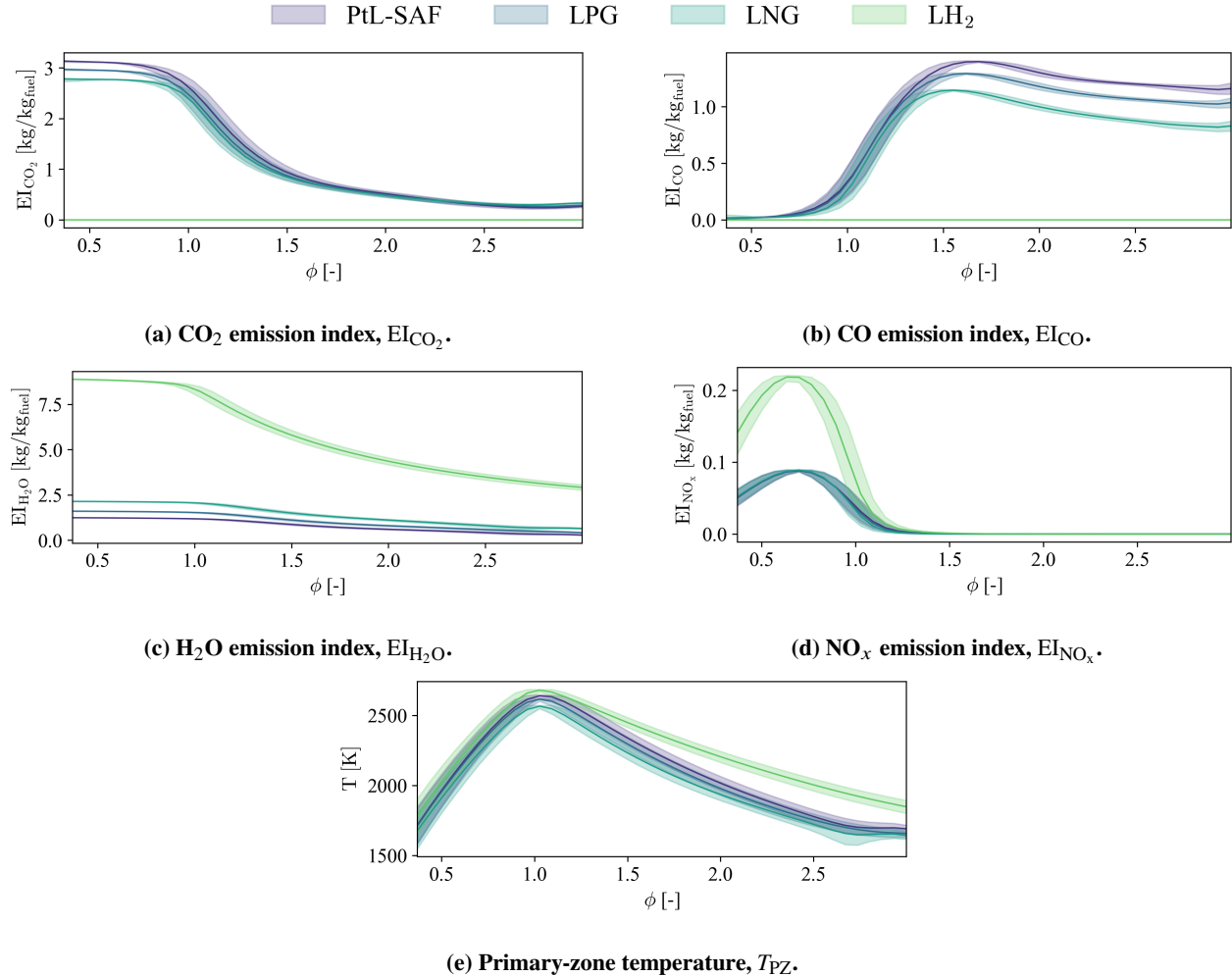


Fig. 18 Primary-zone band plots showing the mean and variability of emission indices and temperature, for PtL-SAF, LPG, LNG, and LH₂.

2. Flight Emissions

Using the modeling framework described above, the total mission-level emissions were estimated for each mild parallel-hybrid A220-100 configuration and compared against the corresponding single-fuel baseline aircraft. The resulting grams of CO_2 -equivalent emissions per revenue passenger kilometer are presented in Fig. 20.

Across all fuel options, the predicted total CO_2e per RPK remains of comparable magnitude, with the LNG configuration yielding the lowest overall value among the fuels considered. These results reflect the combined effects of fuel-specific emission characteristics and aircraft-level penalties, including payload reductions associated with volumetric or mass constraints imposed by alternative fuel storage systems. The comparison between single-fuel and

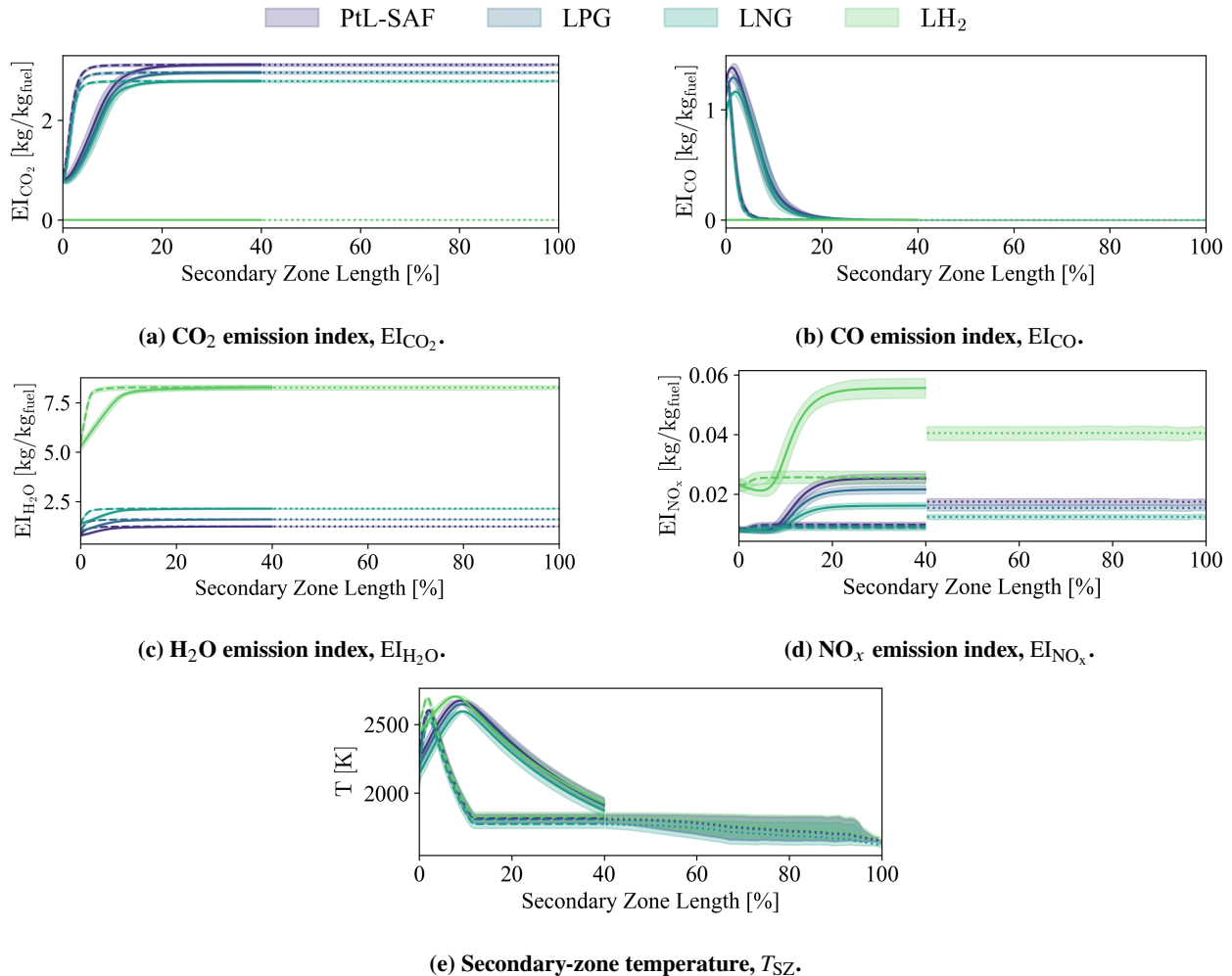


Fig. 19 Secondary-zone band plots showing the mean and variability of emission indices and temperature, for PtL-SAF, LPG, LNG, and LH₂.

hybrid configurations indicates that the introduction of mild hybridization has a limited impact on total mission CO₂ emissions. As shown in Fig. 20, only marginal differences are observed between the single-fuel and hybrid cases for each fuel. This outcome is consistent with the relatively low degree of hybridization considered in this study, for which the electric contribution primarily affects transient, high-power mission segments and does not substantially alter the overall fuel burn across the mission.

Table 8 Monte Carlo uncertainty summary for combustor exit quantities. Mean value, standard deviation, and 5-95% quantile range are reported for each fuel.

Fuel	EI _{CO₂} [kg/kg _{fuel}]	EI _{H₂O} [kg/kg _{fuel}]	EI _{CO} [kg/kg _{fuel}]	EI _{NO_x} [kg/kg _{fuel}]	T _{exit} [K]
PtL-SAF	3.112 ± 0.017	1.238 ± 0.007	$(2.51 \pm 0.45) \times 10^{-4}$	0.0174 ± 0.0006	1654 ± 9
LPG	2.956 ± 0.016	1.594 ± 0.009	$(2.20 \pm 0.41) \times 10^{-4}$	0.0154 ± 0.0006	1648 ± 9
LNG	2.785 ± 0.015	2.137 ± 0.012	$(1.50 \pm 0.22) \times 10^{-4}$	0.0123 ± 0.0005	1621 ± 7
LH ₂	≈ 0	8.259 ± 0.072	≈ 0	0.0405 ± 0.0014	1670 ± 10

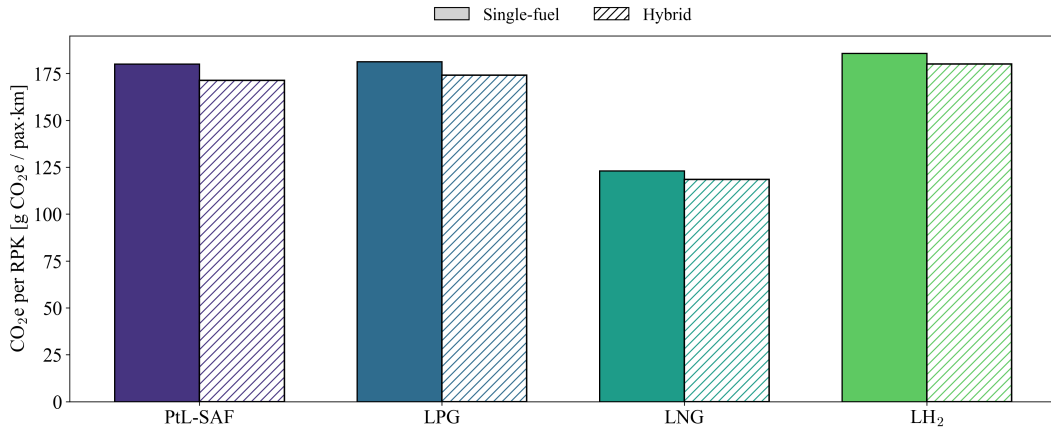


Fig. 20 Flight emissions for different fuels and propulsion architectures.

C. Turnaround Time for Airline Operations

Turnaround time is a critical operational metric for commercial airlines, directly influencing aircraft utilization and schedule robustness, and in the context of hybrid-electric retrofits, it depends not only on passenger and cargo handling but also on the refueling characteristics of each alternative fuel and the time required to recharge the onboard battery pack. To provide a consistent basis for comparison, representative airport refueling rates were adopted from industry sources as shown in Table 9. Battery recharge time was modeled assuming a 1 MW charging capability, aligned with emerging megawatt-class systems for heavy-duty transportation [35].

Table 9 Representative airport refueling rates adopted in this study for modeling turnaround time.

Fuel Type	Fueling Rate [gal/min]	Reference
PtL-SAF	800	[36]
Liquid Petroleum Gas (LPG)	500	[37]
Liquid Natural Gas (LNG)	500	[37]
Liquid Hydrogen (LH ₂)	400	[38]

Figures 21 illustrate the detailed turnaround sequences for the A220-100 configured with each alternative fuel. Each diagram depicts the parallel execution of passenger services, cargo handling, aircraft servicing, and energy replenishment activities, with the overall turnaround time determined by the critical path leading to pushback. Across all fuel configurations, the resulting turnaround time remains comparable, at approximately 42 minutes. For the LPG and LNG variants, the refueling duration increases relative to the PtL-SAF case, rising from approximately 3.3 minutes to about 8.4 minutes. The LH₂ configuration exhibits a substantially longer refueling time of approximately 22.5 minutes. Despite these differences in refueling duration, the turnaround time for all configurations is ultimately constrained by the battery recharging process, which requires approximately 41 minutes. Consequently, even for the mild-hybrid hydrogen retrofit, battery charging remains the primary limiting factor in the turnaround sequence, outweighing the impact of fuel-specific refueling operations.

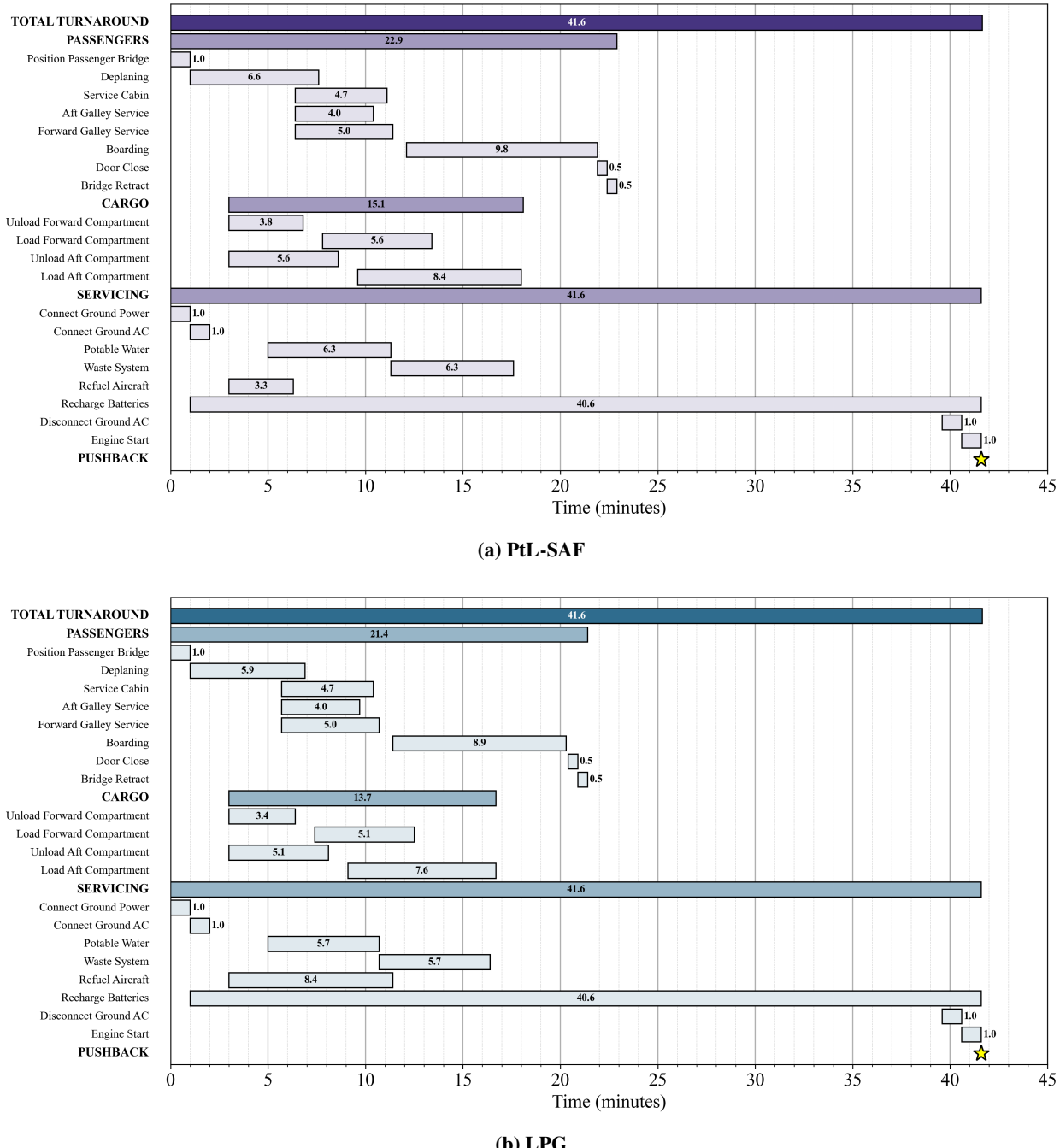


Fig. 21 Turnaround time comparisons for hybrid A220-100 (Part 1 of 2).

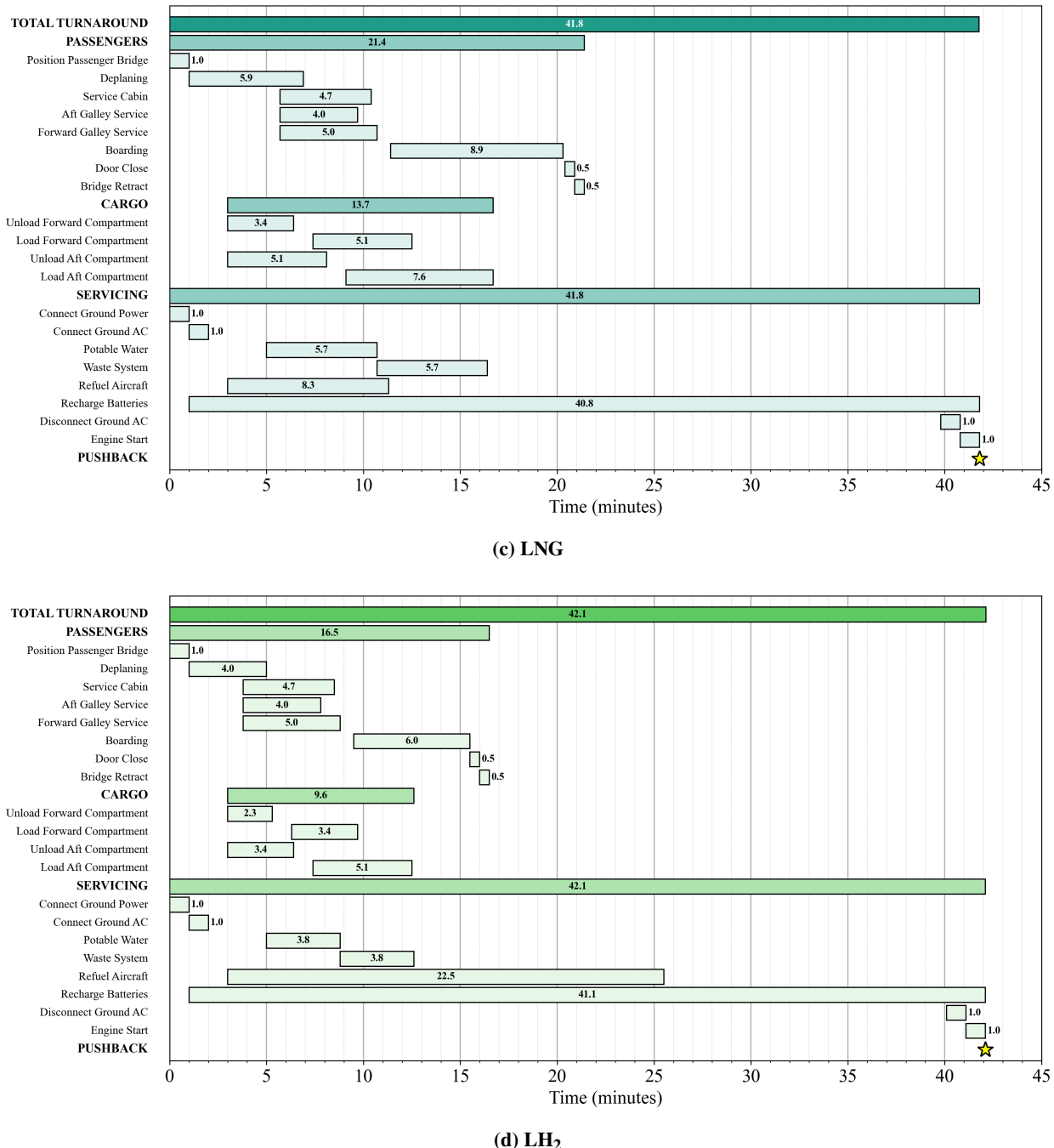


Fig. 21 Turnaround time comparisons for hybrid A220-100 (Part 2 of 2).

VIII. Future Work

The presented study explored the viability of alternative energy retrofits from techno-economic and flight emissions perspectives. While comprehensive, it did not take into account the costs associated with manufacturing and maintaining retrofits, as well as the costs of the various fuel production pathways. Future work seeks to examine this to provide a complete picture of the concept of operations for these low-carbon, liquid-hydrogen fuels. Secondly, future work will seek to relax the outer mold line constraint that was emphasized throughout the paper. As new manufacturing technologies, such as Pultruded Rod Stitched Efficient Unitized Structures, become more advanced and reach higher TRL levels of adoption, it will become easier to construct lightweight, non-cylindrical fuselage cabins that can accommodate more low-density fuels. Lastly, the authors seek to extend this study to other market segments, particularly narrow-body medium-haul flights and wide-body long-haul flights, which account for the majority of aviation-related anthropogenic emissions.

IX. Conclusion

This paper examines challenges in applying hybridization solutions in narrow-body aircraft, focusing on mild parallel hybrid-electric systems using alternative fuels (PtL-SAF, LPG, LNG, and LH₂). The investigation investigates how fuel choice and electrification affect airplane performance, emissions, and operations. The design space is explored using Latin Hypercube Sampling to examine cost per revenue passenger-kilometer, hybridization trends, emissions, and turnaround time. For each configuration, the onboard fuel and energy storage systems are resized within the baseline A220-100 outer mold line to account for mass and volume limits, stability, and certification requirements. The uncertainty associated with the high-fidelity chemical reaction network emissions model was also quantified to strengthen the claims made from flight simulation observations. Findings provide system-level insight into the feasibility and trade-offs of retrofitting existing aircraft with next-generation hybrid-electric and alternative-fuel propulsion technologies. It is shown that the best strategy for hybridization, specifically, the use of an electric motor turbocharger on the low-pressure compressor shaft, mirrors the inverse of specific fuel consumption; that is, it is high during takeoff in the initial climb stages of flight and reaches a minimum during cruise, where the engines are most efficient, before increasing slightly. That said, the benefits of hybridization with existing battery technology are only marginally seen in the case of LH₂ - in most cases, the cost of the single-fuel, non-hybridized aircraft is cheaper on a dollar-per-revenue passenger mile basis. For emissions, mild hybridization results in limited changes in total mission CO₂-equivalent emissions per revenue passenger kilometer relative to single-fuel configurations. For turnaround time, all fuel options yield comparable narrow-body turnaround durations, as battery recharging remains the dominant constraint despite increased refueling times for LPG, LNG, and LH₂.

Acknowledgments

While the trade study conducted in the manuscript is not associated with any sponsored project, the first author wishes to express gratitude for the financial assistance provided by The Boeing Company through Grant: Renewable Energy Pathways and Novel Propulsion Systems for Sustainable Aircraft Concepts (#2024-ETT-PA-102), which was crucial for the development of the emissions models used throughout this work. The second author also wishes to acknowledge the financial support of the NASA Advanced Aircraft Concepts for Environmental Sustainability (AACES) 2050 Program, which supported the development of cryogenic tank models employed for three of the alternative energy fuels.

References

- [1] Owen, B., Lee, D. S., and Lim, L., "Flying into the Future: Aviation Emissions Scenarios to 2050," *Environmental Science Technology*, Vol. 44, No. 7, 2010. <https://doi.org/10.1021/es902530z>, URL <https://pubs.acs.org/doi/full/10.1021/es902530z>.
- [2] UKRI, "A Brief History of Climate Change Discoveries," , 2023. URL <https://www.discover.ukri.org/a-brief-history-of-climate-change-discoveries/index.html>, accessed: 2024-11-20.
- [3] Air Transport Action Group, "Tracking Aviation Efficiency," Accessed via aviationbenefits.org, 2021. URL <https://aviationbenefits.org/downloads/fact-sheet-3-tracking-aviation-efficiency/>, fact Sheet #3.
- [4] Feijoo, F., Iyer, G. C., Avraam, C., Siddiqui, S. A., Clarke, L. E., Sankaranarayanan, S., Binsted, M. T., Patel, P. L., Prates, N. C., Torres-Alfaro, E., and Wise, M. A., "The future of natural gas infrastructure development in the United

- states," *Applied Energy*, Vol. 228, 2018, pp. 149–166. <https://doi.org/10.1016/j.apenergy.2018.06.037>, URL <https://www.sciencedirect.com/science/article/pii/S0306261918309085>.
- [5] Rendón, M. A., Sánchez, R. C. D., Gallo, M. J., et al., "Aircraft Hybrid-Electric Propulsion: Development Trends, Challenges and Opportunities," *Journal of Control, Automation and Electrical Systems*, Vol. 32, 2021, pp. 1244–1268. <https://doi.org/10.1007/s40313-021-00740-x>.
 - [6] Pornet, C., Gologan, C., Vratny, P. C., Seitz, A., Schmitz, O., Isikveren, A. T., and Hornung, M., "Methodology for Sizing and Performance Assessment of Hybrid Energy Aircraft," *Journal of Aircraft*, Vol. 52, No. 1, 2015, pp. 341–352. <https://doi.org/10.2514/1.C032716>.
 - [7] U.S. Department of Transportation, Bureau of Transportation Statistics, "T-100 Segment (All Carriers) – 2024 Data," https://transtats.bts.gov/DL_SelectFields.aspx?gnoyr_VQ=FMG&QO_fu146_anzr=Nv4+Pn44vr45, 2024. URL https://transtats.bts.gov/DL_SelectFields.aspx?gnoyr_VQ=FMG&QO_fu146_anzr=Nv4+Pn44vr45, downloaded on December 02, 2025. Includes segment-level traffic and capacity data for all U.S. and foreign carriers operating domestic flights in 2024.
 - [8] Airbus, "A220 Aircraft Characteristics Airport and Maintenance Planning," , Jun. 2025. URL <https://www.aircraft.airbus.com/en/customer-care/fleet-wide-care/airport-operations-and-aircraft-characteristics/aircraft-characteristics>.
 - [9] The Boeing Company, "Boeing 737 Root Airfoil," <http://airfoiltools.com/airfoil/details?airfoil=b737a-il>, 2025. Accessed: 2025-12-13.
 - [10] The Boeing Company, "Boeing 737 Midspan Airfoil," <http://airfoiltools.com/airfoil/details?airfoil=b737b-il>, 2025. Accessed: 2025-12-13.
 - [11] The Boeing Company, "Boeing 737 Midspan Airfoil (b737c-il)," <http://airfoiltools.com/airfoil/details?airfoil=b737c-il>, 2025. Accessed: 2025-12-13.
 - [12] The Boeing Company, "Boeing 737 Outboard Airfoil (b737d-il)," <http://airfoiltools.com/airfoil/details?airfoil=b737d-il>, 2025. Accessed: 2025-12-13.
 - [13] FlightAware, "Live Flight Tracking," <https://www.flightradar24.com/live/>, 2025. Accessed: 2025-12-13.
 - [14] LEADS Group, "RCAIDE: Open-source Python environment for electrified aircraft design," <https://github.com/leadsgroup/RCAIDE>, 2024. Accessed: 2024-11-13.
 - [15] Cantwell, B. J., "AA283 Course Reader: Aircraft and Rocket Propulsion," Unpublished course reader, Jan. 2021. Department of Aeronautics and Astronautics, Stanford University. Course notes, not publicly distributed.
 - [16] Goodwin, D. G., Moffat, H. K., Schoegl, I., Speth, R. L., and Weber, B. W., "Cantera: An object-oriented software toolkit for chemical kinetics, thermodynamics, and transport processes," <https://www.cantera.org>, 2023. <https://doi.org/10.5281/zenodo.8137090>, version 3.0.0.
 - [17] Brink, L. F. J., "Modeling the impact of fuel composition on aircraft engine NOx, CO and soot emissions," Master's Thesis, Massachusetts Institute of Technology, Cambridge, MA, 2020.
 - [18] Allaire, D. L., "A physics-based emissions model for aircraft gas turbine combustors," S.M. Thesis, Massachusetts Institute of Technology, Dept. of Aeronautics and Astronautics, Cambridge, MA, Jun. 2006. URL <https://dspace.mit.edu/handle/1721.1/35584>, advisor: Karen Willcox and Ian Waitz.
 - [19] Chowdhury, G. M., and Yu, F., "A 0D aircraft engine emission model with detailed chemistry and soot microphysics," *Combustion and Flame*, Vol. 159, No. 4, 2012, pp. 1670–1686. <https://doi.org/10.1016/j.combustflame.2011.11.006>, URL <https://doi.org/10.1016/j.combustflame.2011.11.006>.
 - [20] Lefebvre, A. H., and Ballal, D. R., *Gas Turbine Combustion: Alternative Fuels and Emissions*, 3rd ed., CRC Press, 2010.
 - [21] Wang, Z., De Breuker, R., Sodja, J., Wolleswinkel, R. E., de Vries, R., and Giuffré, A., "A study on wing structural design and sizing for a large battery-electric aircraft," *AIAA Aviation Forum and Ascend 2025*, 2025, p. 3470.
 - [22] Gillies, S., van der Wel, C., Van den Bossche, J., Taves, M. W., Arnott, J., Ward, B. C., et al., "Shapely," Zenodo, 2024. <https://doi.org/10.5281/zenodo.10982792>, URL <https://doi.org/10.5281/zenodo.10982792>.
 - [23] Mukhopadhyaya, J., and Rutherford, D., "Performance Analysis of Evolutionary Hydrogen-Powered Aircraft," <https://theicct.org/wp-content/uploads/2022/01/LH2-aircraft-white-paper-A4-v4.pdf>, 2022. URL <https://theicct.org/wp-content/uploads/2022/01/LH2-aircraft-white-paper-A4-v4.pdf>, find definition on page 3.

- [24] Administration, F. A., “Advisory Circular: Design Considerations for Minimizing Hazards Caused by Uncontained Turbine Engine and Auxiliary Power Unit Rotor Failure,” https://www.faa.gov/documentLibrary/media/Advisory_Circular/AC_20-128A.pdf, 1997. URL https://www.faa.gov/documentLibrary/media/Advisory_Circular/AC_20-128A.pdf.
- [25] Administration, F. A., “Advisory Circular: Emergency Evacuation Demonstrations,” https://www.faa.gov/documentLibrary/media/Advisory_Circular/AC_25.803-1A.pdf, 2012. URL https://www.faa.gov/documentLibrary/media/Advisory_Circular/AC_25.803-1A.pdf.
- [26] Agency, E. U. A. S., “Easy Access Rules for Large Aeroplanes (CS-25),” <https://www.easa.europa.eu/en/document-library/easy-access-rules/online-publications/easy-access-rules-large-aeroplanes-CS-25?page=25>, 2023. URL <https://www.easa.europa.eu/en/document-library/easy-access-rules/online-publications/easy-access-rules-large-aeroplanes-CS-25?page=25>, sUBPART D – DESIGN AND CONSTRUCTION: CS 25.721 General.
- [27] of Energy, U. D., “Hydrogen Storage,” <https://www.energy.gov/eere/fuelcells/hydrogen-storage>, 2025. URL <https://www.energy.gov/eere/fuelcells/hydrogen-storage>.
- [28] Zabetakis, M. G., *Safety with Cryogenic Fluids*, Plenum Press, New York, New York, 1967. Includes data on Liquid Nitrogen and Hydrogen.
- [29] Wells, D. P., Horvath, B. L., and McCullers, L. A., “The Flight Optimization System Weights Estimation Method,” Tech. Rep. NASA/TM-2017-219627/VOL1, NASA Langley Research Center, Hampton, VA, United States, 2017. URL <https://ntrs.nasa.gov/citations/20170005851>, technical Memorandum, NF1676L-27097, L-20820. Public Use Permitted.
- [30] IHS Jane’s, i. b., “IHS Jane’s aero-engines.” , 2013 - 2017.
- [31] FTI Consulting, “eSAF Stands Ready for Takeoff,” <https://www.fticonsulting.com/insights/articles/esaf-stands-readytakeoff>, Nov. 2024. URL <https://www.fticonsulting.com/insights/articles/esaf-stands-readytakeoff>, accessed: Dec. 14, 2025.
- [32] U.S. Department of Energy, Alternative Fuels Data Center, “Alternative Fuel Price Report and Fuel Prices,” <https://afdc.energy.gov/fuels/prices.html>, 2025. URL <https://afdc.energy.gov/fuels/prices.html>, accessed: Dec. 14, 2025.
- [33] International Council on Clean Transportation (ICCT), “The Price of Green Hydrogen: Estimated Future Production Costs,” <https://theicct.org/the-price-of-green-hydrogen-estimate-future-production-costs-may24/>, 2024. URL <https://theicct.org/the-price-of-green-hydrogen-estimate-future-production-costs-may24/>, accessed: 2025-12-14.
- [34] Guidotti, M., Gupta, R., Dost, J., Mehta, D., Kolar, A., Zhang, C., Ansell, P., and Clarke, M., “The Impact of Alternative Fuels on U.S. Domestic Aviation Emissions,” *AIAA AVIATION FORUM AND ASCEND*, 2025, American Institute of Aeronautics and Astronautics Inc, AIAA, 2025. <https://doi.org/10.2514/6.2025-3102>.
- [35] EVChargingStations.com, “Siemens Megawatt Charging System,” <https://evchargingstations.com/chargingnews/siemens-megawatt-charging-system/>, 2025. Accessed: 2025-12-13.
- [36] BETA Fueling Systems, “Hydrant Dispenser Cart for Commercial Aviation,” <https://betafueling.com/industries/commercial-aviation/hydrant-dispenser-cart/>, 2025. Accessed: 2025-12-13.
- [37] Sharafian, A., Herrera, O. E., and Mérida, W., “Performance analysis of liquefied natural gas storage tanks in refueling stations,” *Journal of Natural Gas Science and Engineering*, Vol. 36, 2016, pp. 496–509. <https://doi.org/10.1016/j.jngse.2016.10.062>, URL <https://www.sciencedirect.com/science/article/pii/S1875510016308009>.
- [38] International Council on Clean Transportation (ICCT), “Quick Pit Stops: A Challenge for Zero-Emission Planes,” <https://theicct.org/quick-pit-stops-a-challenge-for-zero-emission-planes/>, 2025. Accessed: 2025-12-13.